UNIVERSITY OF CALIFORNIA, MERCED

Rare Earth Ions and Quantum Dots as Local Optical Probes of Electromagnetic Coupling in 2D and 3D Systems

A dissertation submitted in partial satisfaction of the requirements
for the degree of Doctor of Philosophy

in

Physics

by

Christopher George Louis Ferri

Committee in charge:

Professor Michael Scheibner, Chair

Professor Lin Tian

Professor Sayantani Ghosh

2015

The Dissertation of Christopher George Louis Ferri is approved, and it is acceptable in quality and form for publication on microfilm and electronically:

Professor Lin Tian — Date

Professor Sayantani Ghosh — Date

Professor Michael Scheibner, Chair — Date

University of California, Merced
2015

This work is dedicated to:

- my family, who have supported my passion for Physics since I was but a wee lad;
- Dr. Sayantani Ghosh, who has been the single greatest driving force behind my education as a scientist; and
- my friends, without whom I could have completed my work in a timely fashion.

Contents

List of Symbols

α	Absorptivity
ω	Angular Frequency
a_0	Bohr Radius
k_B	Boltzmann's Constant
ν_0	Center Wavenumber
CSW	Cumulative Spectral Weight
Θ_{cw}	Curie-Weiss Temperature
T_D	Debye Temperature
ε_0	Electric Constant
$\mathbf{D}$	Electric Dipole Vector
Φ	Electric Potential
m_e	Electron Mass
E	Energy
ξ	Exchange Integral
f	Focal Length
e	Fundamental Unit of Charge
$\mathcal{H}$	Hamiltonian
Γ	Homogeneous Linewidth
n	Index of Refraction
Υ	Inhomogeneous Linewidth
τ	Lifetime
$\boldsymbol{\mu}$	Magnetic Dipole Vector
$\mathbf{p}$	Momentum
m_N	Nuclear Mass
NA	Numerical Aperture
OD	Optical Density Units
μ	Reduced Mass
a_μ	Reduced Radius
S_0	Reference Spectrum
SW	Spectral Weight
S_{trans}	Spectrum Measured in Transmission
c	Speed of Light
σ	Standard Deviation
λ	Wavelength
ν	Wavenumber

List of Figures

List of Tables

Acknowledgements

In the spring of 2006, I entered the University of California's Merced campus. I had just tasted real physics for the first time in high school and was eager to continue my education in that field. At the same time, Dr. Sayantani Ghosh was moving to UC Merced from her postdoc to be a professor. Serendipitously, she found me–a wet-behind-the-ears, first-year undergraduate–and offered me a research position in her lab. That was nearly nine years and two higher education degrees ago.

Sai and I built the Ghosh Lab at UC Merced from the empty room it was in 2006 to the top flight microscopy and spectroscopy lab it is today in 2015. I am incredibly thankful for the opportunity to experience the building of a lab and subsequently being able to work there for my doctorate. I was basically given the opportunity to customize my graduate research experience, and it has been one of the most rewarding experiences of my life. Thank you very much, Sai, for being such an amazing mentor and friend, and thank you for gambling on me by hiring me so early in my college career. You have truly changed my life.

I must also thank Robert Baker, my high school physics teacher. Baker is one of the best teachers I have ever had. In my role as a teacher, I have tried to emulate his teaching techniques; he made physics fun for those who were uninterested and was selfless with regards to nurturing scientific minds. One of the best memories I have is of constructing the marble factory as a high school student and then returning to El Camino High School as a graduate student to be a judge for the marble factory project. I am lucky to have had Robert Baker as a teacher, and I now count myself fortunate to have him as a friend.

While I am acknowledging my educators, I would also like to thank the professors in the Math and Physics departments at the University of California, Merced. In particular from the Physics Department, I would like to thank Jay Sharping, Kevin Mitchell, Ajay Gopinathan, Michael Scheibner, Lin Tian and Haik Stepanian. In the Math Department, I am most grateful to Arnold Kim, Harish Bhat and Khaz Brito. All of these people have invested time and effort into my scientific development. Jay, Kevin, Ajay and Arnold were some of UC Merced's first or original faculty. They were there with me in the beginning (when the campus was still new) and because of the intimacy that resulted from small class sizes, I see them more as peers than my superiors, which is a very empowering feeling. Harish has been a wonderful resource for understanding statistics, and our conversations directly contributed to the work in this dissertation. I am also thankful to have him as a compatriot during the recent highs and lows of the San Francisco Giants. Haik and Khaz were teaching assistants for several of my physics and math classes while I was an undergraduate. They directly shaped my education, and the conversations we had were particularly valuable to under-

standing topics related to my research. They have also been good friends. Michael and Lin have not only been my educators (particularly in the field of quantum mechanics) but also my dissertation committee members. They deserve special recognition for their guidance during my graduate education and their ability to sit through my research presentations. They have been fair and thoughtful, and I could not think of anyone better to be the stewards of my career as a graduate student.

I would also like to thank my family, particularly my mom and dad (Susan and Guy) and my sister, Natalie. I have wanted to be a physicist since I was in fourth grade. The goal I have had for most of my life is to attain the title of Doctor of Philosophy in Physics. My family fully supported me in that endeavor by nurturing my love of science by taking me to science museums like San Francisco's Exploratorium and giving me more books and videos about physics and science than I could possibly read during my childhood. I am very happy that I have been able to return their unwavering support with real progress toward my life's goals. I am particularly proud because I am a first generation immigrant on my father's side, and I am the first person in his family to reach this level of scholastic achievement. I am truly lucky to have such a supportive and loving family.

I would like to acknowledge the efforts of Richard Inman, Brent Rich, Ajay Gopinathan, Michelle Khine and Sai Ghosh who coauthored the study which comprises Chapter 5. This study was published in the journal *Optical Materials Express* [19] with funding from the National Science Foundation.

I would also like to acknowledge Michael Tennenbaum, Jacky Wan and Sai Ghosh who are coauthors on the study which comprises Chapter 6 and which is currently being prepared for publication. I would also like to acknowledge Dr. Thomas Rosenbaum's group from the University of Chicago with whom we collaborated to take AC Magnetic Susceptibility measurements on the neodymium doped gadolinium gallium garnet crystals investigated in this study [99]. This work was also funded by the National Science Foundation.

Lastly, I thank Dr. Sayantani Ghosh, Dr. Lin Tian, Dr. Michael Scheibner and Susan Steffes-Ferri for graciously editing this dissertation.

Curriculum Vitae

Academic Progress

Standing: Ph.D. Candidate

Principle Investigator: Sayantani Ghosh

Field: Condensed Matter Physics

Current GPA: 3.665

Education

2010-2015: Doctor of Philosophy, Physics, University of California, Merced, California

2006-2010: Bachelor of Science, Physics, University of California, Merced, California

Publications

1. Ferri, C. G. L., J. C. Wan, M. Tennenbaum, and S. Ghosh Spectroscopic Signature of the Spin Liquid Phase of Neodymium doped Gadolinium Gallium Garnet. *(In Progress).*

2. Woo, N., Silevitch, D. M., Ferri, C., Ghosh, S., & Rosenbaum, T. F. (2015). Interplay of disorder and geometrical frustration in doped gadolinium gallium garnet. Journal of Physics: Condensed Matter, 27(29), 296001.

   doi:10.1088/0953-8984/27/29/296001

3. Amaral, Jose Jussi, Jacky Wan, Andrea L. Rodarte, Christopher Ferri, Makiko T. Quint, Ronald J. Pandolfi, Michael Scheibner, Linda S. Hirst, and Sayantani Ghosh. 2015. Magnetic Field Induced Quantum Dot Brightening In Liquid Crystal Synergized Magnetic And Semiconducting Nanoparticle Composite Assemblies. *Soft Matter* 11 (2): 255-260.

   doi:10.1039/c4sm02015d.

4. Ferri, C. G. L., R. H. Inman, B. Rich, A. Gopinathan, M. Khine, and S. Ghosh. 2013. Plasmon-Induced Enhancement Of Intra-Ensemble FRET In Quantum Dots On Wrinkled Thin Films. *Optical Materials Express* 3 (3): 383.

doi:10.1364/ome.3.000383.

5. Rodarte, A. L., C. G. L. Ferri, C. Gray, L. S. Hirst, and S. Ghosh. 2012. Directed Assembly And In Situ Manipulation Of Semiconductor Quantum Dots In Liquid Crystal Matrices. *Emerging Liquid Crystal Technologies VII.*

   doi:10.1117/12.906235.

6. Verma, Y. K., R. H. Inman, C. G. L. Ferri, H. Mirafzal, S. N. Ghosh, D. F. Kelley, L. S. Hirst, S. Ghosh, and W. C. Chin. 2010. Electrical Modulation Of Static And Dynamic Spectroscopic Properties Of Coupled Nanoscale Gase Quantum Dot Assemblies. *Physical Review B* 82 (16).

   doi:10.1103/physrevb.82.165428.

7. Ghosh, S. N., B. B. Buckley, C. G. L. Ferri, X. Li, F. M. Mendoza, Y. K. Verma, N. Samarth, D. D. Awschalom, and S. Ghosh. 2010. Polarization Based Control Of Optical Hysteresis In Coupled Gaas Microdisks. *Applied Physics Letters* 97 (1): 011106.

   doi:10.1063/1.3462309.

8. Fu, Chi-Cheng, Anthony Grimes, Maureen Long, Christopher G. L. Ferri, Brent D. Rich, Somnath Ghosh, Sayantani Ghosh, Luke P. Lee, Ajay Gopinathan, and Michelle Khine. 2009. Tunable Nanowrinkles On Shape Memory Polymer Sheets. *Adv. Mater.* 21 (44): 4472-4476.

   doi:10.1002/adma.200902294.

Presentations

1. Ferri, Christopher, and Sayantani Ghosh A comparison of homogeneous and inhomogeneous absorption broadening in Nd doped Gadolinium Gallium Garnet. American Physical Society, March Meeting 2015. Henry B. Gonzalez Convention Center, San Antonio. 6 Mar. 2015.

2. Ferri, Christopher, Jacky Wan, Michael Tennenbaum, and Sayantani Ghosh. A concentration dependence of the low temperature fluorescence of Neodymium (III) doped Gadolinium Gallium Garnet. American Physical Society, March Meeting 2014. Colorado Convention Center, Denver. 6 Mar. 2014.

3. Ferri, Christopher, Chris Weibe, and Sayantani Ghosh. "NIR Optical Studies of the Warped-Kagome Frustrated Magnet Neodymium Langasite." American Physical Society, March Meeting 2013. Convention Center, Baltimore. 22 Mar. 2013.

4. Ferri, Christopher, Michael Tennenbaum, and Sayantani Ghosh. "Spectral Signature of Neodymium Dopants in Frustrated Gadolinium Gallium Garnet Lattice." American Physical Society, March Meeting 2012. Convention Center, Boston. 1 Mar. 2012.

5. Ferri, Christopher, Anthony Grimes, and Sayantani Ghosh. "Colloidal Quantum Dot Red-Shifting on Textured Metal Surfaces." American Physical Society, March Meeting 2011. Convention Center, Dallas. 23 Mar. 2011.

6. Ferri, Christopher, Somnath Ghosh, Brent Rich, Michelle Khine, and Sayantani Ghosh. "The Effect of Roughened Metallic Films on Colloidal Quantum Dot Energy Transfer." American Physical Society, March Meeting 2009. David L. Lawrence Convention Center, Pittsburgh. 20 Mar. 2009.

7. Ferri, Christopher, M. Gallardo, Y. Verma, D. Kelley, and S. Ghosh. "Self Assembling Quantum Dot Aggregates in Liquid Crystal Matrices." American Physical Society, March Meeting 2008. Morial Convention Center Room, New Orleans. 10 Mar. 2008.

Abstract

Rare Earth Ions and Quantum Dots as Local Optical Probes of Electromagnetic Coupling in 2D and 3D Systems

by

Christopher George Louis Ferri

Doctor of Philosophy in Physics

University of California, Merced

Michael Scheibner, Chair

Isolated ions and nanoparticles are well understood, and the quantum mechanics that describes their behavior is well developed. Thus, these objects are ideal as probes for systems whose properties are poorly understood. This thesis is concerned with developing an understanding of the electronic and optical properties of rare earth ions and semiconductor nanoparticles and using them as probes. Particularly, we use what is understood about these probes to remove the effects of well understood processes from experimental data. The resulting processed data contains information about the system being probed via that system's influence on the probe.

This thesis presents two experimental studies. The first is the investigation of the presence of localized surface plasmons on a wrinkled gold-palladium surface. We deposit semiconductor nanoparticles on this surface and subsequently measure the optical properties of the nanoparticles to identify signatures of plasmon-nanoparticle coupling. We then discuss this coupling in the context of solar energy harvesting. The second study is an investigation of the geometrically frustrated magnetic phase (spin liquid) of gadolinium gallium garnet. We dope this crystal with a rare earth, trivalent neodymium, which is optically active. We then track the infrared emission spectrum of the dopant for signatures of neodymium/spin-liquid coupling. We then discuss the optical effects measured in the context of measuring and manipulating the spin-protectorate magnetic phase of gadolinium gallium garnet.

Chapter 1

Introduction

One of the greatest successes of quantum mechanics has been the description of atomic systems from first principles, which allows for the prediction of physical properties rather than the phenomenological approaches used to describe the vast majority of systems prior to its invention. With the invention of computers came the ability to model the behavior of multi-electron systems with high accuracy. The main thrust of atomic and condensed matter physics in the decades prior to the year 2000 have been refining models and understanding isolated or weakly coupled atomic systems.

Due to our maturity in understanding the uncoupled and weakly coupled systems, modern condensed matter physics has been increasingly interested in the theoretical and experimental study of strongly coupled electronic systems. Strongly coupled electronic systems promise a new frontier in computing and energy harvesting and transmission.

In this thesis, we will discuss experimental studies utilizing well understood, optically active atomic and nanoparticle systems as probes for poorly understood coupled systems, with the primary aim being to use the probe's optical properties to extract information about a system. The fundamental technique we use in these studies is ultraviolet-visible-near-infrared spectroscopy, which provides information about the state of our probes and how that state deviates from their uncoupled behavior. We will study the electromagnetic properties of two systems: the first is a study of the plasmonic properties of a wrinkled metal surface and the second is a study of the magnetic dynamics of a material with a spin liquid phase which is a geometrically frustrated magnetic phase.

Plasmon Active Surfaces

Plasmons, coherent excitation of a metal's conduction electrons, have recently been a particularly active research topic due to their technological applications in optics and sensing. They have been used in optical applications to image objects smaller than the classical resolution of optics, called the diffraction limit, using a device called a plasmonic lens [38]. In addition, they have been used in designs of optical waveguides for optical computing applications [91]. In the realm of sensing, they have been used to increase the detection sensitivity of Raman spectroscopy to the single molecule limit via a process known as Surface Enhanced Raman Scattering (SERS) [83]. We will investigate a wrinkled metal surface to determine its potential application for SERS and solar energy harvesting.

The surfaces we will discuss are interesting because they are self-patterning and quickly fabricated using inexpensive materials.

Spin Liquids

A geometrically frustrated magnetic system is one in which the magnetic moments of the system have a preferential alignment, but are unable to align due to the geometry of the lattice they are in. There are several magnetic phases that fall under this description. The one we discuss here is called a spin liquid. An understanding of the spin liquid phase theoretically and experimentally is important to developments in a general class of problems known as topologically frustrated systems, for example topological frustration in protein folding [85]. An understanding of spin liquids does not just relate to frustrated systems, it is also a way to study superconductivity. The spin dimer ordering seen in spin liquid phases is directly related to cooper pairing in superconductors [43]. Lastly, spin liquid materials could potentially be a platform for quantum computation due to pseudo-particle excitations allowed by the magnetic disorder [40, 67].

Here we will discuss gadolinium gallium garnet. This material has a spin liquid phase, which was discovered in measurements of specific heat [15, 47, 79], AC magnetic susceptibility [32, 79], muon-spin relaxation [60] and neutron scattering [70, 102]. Furthermore, it has a unique spin protectorate magnetic phase [23] which might be useful for implementing quantum computing protocols. The previously discussed measurements are not capable of addressing individual protectorates, because they are non-local techniques. Here we discuss the development of an optical probe technique which could be used to measure the properties and address spin protectorates locally.

Overview

Before we discuss these studies, we will first explore what is understood about the electronic properties of rare earth ions and semiconductor nanoparticles and how those properties manifest optically. Chapter 2 will be an introduction into calculating and modeling the time-independent electronic states of atoms, ions and nanoparticles. In Chapter 3, we will discuss how transitions between these states are modeled. This will result in a description of the experimental signatures of these transitions and what to look for when using these systems as probes. Chapter 4 is concerned with the experimental methods used to study systems spectroscopically.

In the last two chapters, we will discuss experiments on systems with coupling. Chapter 5 will detail the experimental analysis of a system which supports localized surface plasmons using semiconductor nanoparticles to confirm their presence and the implications of the coupling between plasmons and nanoparticles to solar energy collection and bio-sensing. Chapter 6 will discuss the spectroscopy of trivalent neodymium coupled to the spin liquid phase of gadolinium gallium garnet crystals. This chapter will primarily focus on the optical properties of neodymium in the presence of a spin liquid. In addition, we will also discuss the impact of this type of experiment on the detection and diagnosis of other magnetic phases.

Chapter 2

Electronic Structure of Rare Earth Ions and Semiconductor Nanoparticles

We begin with a discussion of the quantum states atoms and nanoparticles have. By finding a quantum description of these systems, we gain an understanding of how their electronic and magnetic properties manifest optically. Specifically, we will find that atoms in the Lanthenide series (rare earth atoms) have interesting electronic states that isolate them from vibrations while simultaneously being sensitive to magnetic fields and that semiconductors have discrete states similar to atoms when their dimensions are reduced to nanometer scales. These properties enable us to use these systems as optical probes in the studies discussed in the last two chapters.

2.1 Rare Earth Ions

A quantum description of spectroscopy requires a full treatment of the time dependent Schrödinger equation. To begin this analysis, we will first identify the solutions of the time independent Hamiltonian of multi-electron atoms, which allows us to determine the stationary states of the electrons in the ion of interest. The full time-dependent solution will then allow us to determine what happens when transitions between these states, or energy levels, occurs.

2.1.1 Single Electron Wavefunctions

An analysis of atoms in general requires a mathematical program that begins with the wavefunctions describing a single electron in a Coulomb potential and builds up to correlated multi-electron wavefunctions via a linear combination of single electron wavefunctions and series of approximations resulting in the addition of perturbations to what is effectively the single electron Hamiltonian.

We begin with the Hamiltonian of a single electron in the spherically symmetric Coulomb potential of a nucleus with Z number of protons and nuclear mass M in a co-moving reference frame:

$$\mathcal{H} = \frac{\mathbf{p}^2}{2\mu} - \frac{Ze^2}{4\pi\varepsilon_0 r} = \frac{-\hbar^2}{2\mu}\boldsymbol{\nabla}^2 - \frac{Ze^2}{4\pi\varepsilon_0 r}, \tag{2.1}$$

where $\mathbf{p}$ is the momentum of the electron orbiting the nucleus, μ is the reduced mass of the system, and r is the radius of the electron relative to the position of the nucleus. The eigenfunctions of this time-independent Hamiltonian satisfy Schrödinger's equation

$$\mathcal{H}\Psi(\mathbf{r}) = E\Psi(\mathbf{r}), \tag{2.2}$$

where E is the eigenvalue associated with some eigenfunction $\Psi(\mathbf{r})$, which in this context are referred to as the energy and energy state of the electron. The eigenfunctions of this Hamiltonian are the well known hydrogenic wavefunctions, the derivation of which have been detailed in many publications [11, 20, 30, 86]:

$$\Psi_{n,l,m_l}(r,\theta,\phi) = R_{nl}(r)Y_l^{m_l}(\theta,\phi), \tag{2.3}$$

where $R_{nl}(r)$ is

$$R_{nl}(r) = \sqrt{\left(\frac{2Z}{na_\mu}\right)^3 \frac{(n-l-1)!}{2n[(n+l)!]}}\left(\frac{2Zr}{na_\mu}\right)^l \exp\left(\frac{-Zr}{na_\mu}\right) L_{n-l-1}^{2l+1}\left(\frac{2Zr}{na_\mu}\right), \tag{2.4}$$

$$a_\mu = \frac{m_e a_0}{\mu}, \tag{2.5}$$

$$\mu = \frac{m_N m_e}{m_N + m_e}, \tag{2.6}$$

where L_{n-l-1}^{2l+1} are the associated Laguerre polynomials, m_N is the nuclear mass, m_e is the electron mass, and a_0 is the Bohr radius. $Y_l^{m_l}(\theta,\phi)$ are the spherical harmonics. The eigenenergy of this solution is

$$E_n = \frac{-Z^2\hbar^2}{2\mu n^2 a_\mu^2}. \tag{2.7}$$

The parameters n, l and m_l are the quantum numbers for the hydrogen-like atom. n is the energy level and is an integer between 1 and infinity. l is the orbital angular momentum quantum number associated with the total angular momentum operator $\mathbf{l}^2$ and takes integer values $0 \ldots n-1$. In spectroscopy these values are labeled by letters where $l = 0$, 1, 2, 3, 4, 5... corresponds to s, p, d, f, g, h... The last quantum number m_l is called the magnetic quantum number which quantizes the z-axis projection of the angular momentum operator l_z, it takes values $-l, -l+1 \ldots l-1, l$. Examples of the radial probability distribution of the electron's position are given in figure 2.1 and examples of the spherical harmonics are given in figure 2.2.

This does not complete our description of hydrogen-like atoms. We must also include the spin of the electron in the wavefunction. The associated operator is $\mathbf{s}^2$ with quantum number s and magnetic quantum number m_s associated with the z-axis projection of the spin. Electrons are spin-1/2 particles so the total spin is always 1/2 for a single electron, and m_s is either 1/2 (up) or $-1/2$ (down). The eigenstates are spin vectors typically labeled α and β respectively:

$$|s = 1/2, m_s = 1/2\rangle = |\alpha\rangle = \begin{pmatrix} 1 \\ 0 \end{pmatrix} \tag{2.8}$$

$$|s = 1/2, m_s = -1/2\rangle = |\beta\rangle = \begin{pmatrix} 0 \\ 1 \end{pmatrix}. \tag{2.9}$$

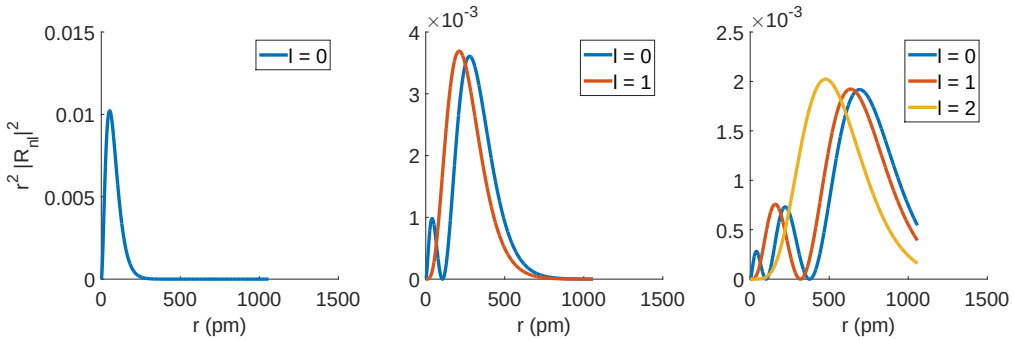

Figure 2.1: The radial probability density of the (left) n = 1, (middle) n = 2 and (right) n = 3 states of hydrogen.

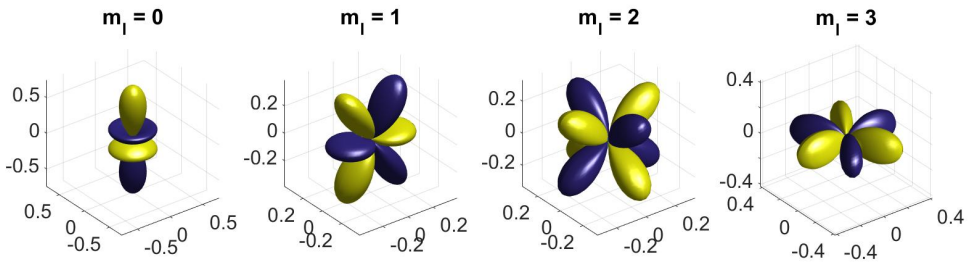

Figure 2.2: The real value of $Y_3^{m_l}(\theta, \phi)$, where blue values are negative and yellow positive.

Thus, the complete description of the single electron atom is a product of orbital and spin states

$$u_{n,l,m_l,m_s}(\mathbf{r}) = |n, l, m_l, s, m_s\rangle = |n, l, m_l, m_s\rangle = \Psi_{n,l,m_l}(r, \theta, \phi)\,|s, m_s\rangle\,, \tag{2.10}$$

where the spin quantum number is typically dropped because it can only take the value $1/2$. This completes our description of the single electron atom. All subsequent refinements to the hydrogen-like Hamiltonian will be considered perturbations which will result in state-mixing between these hydrogenic wavefunctions.

The first correction we must consider is spin-orbit coupling, which is a special relativistic correction that is particularly important for rare earth ions because, as we will see later, the multi-electron states of rare earths are linear combinations of the spin-orbit coupled states. The spin-orbit Hamiltonian is [26, 77]

$$\mathcal{H}_{\text{SO}} = \zeta(r)\mathbf{l}\cdot\mathbf{s} = \zeta(r)(l_x s_x + l_y s_y + l_z s_z), \tag{2.11}$$

$$\zeta(r) = \frac{Ze^2}{8\pi\varepsilon_0 m^2 c^2 r^3}. \tag{2.12}$$

Thus, because l_z and s_z do not commute with the other components, x and y, of the angular momentum operators, they also do not commute with the spin-orbit Hamiltonian. This indicates that the hydrogenic wavefunctions we derived initially are not eigenstates of the spin-orbit Hamiltonian. We can construct a new operator that resolves this issue:

$$\mathbf{j} = \mathbf{l} + \mathbf{s}. \tag{2.13}$$

We call $\mathbf{j}$ the total angular momentum. We can now rewrite the spin-orbit Hamiltonian in terms of the total angular momentum:

$$\mathcal{H}_{\mathrm{SO}} = \frac{1}{2}\zeta(r)(\mathbf{j}^2 - \mathbf{l}^2 - \mathbf{s}^2). \tag{2.14}$$

These angular momentum operators all commute with each other and the hydrogenic Hamiltonian, so constructing the appropriate eigenstates of this operator will also be a valid basis for the hydrogenic Hamiltonian. The cost of being able to diagonalize this system is the construction of a more complicated set of basis states, which have quantum number j which can take values $|l-s|, |l-s|+1, ..., l+s-1, l+s$ associated with the $\mathbf{j}^2$ operator and magnetic quantum number m_j which takes values $-j, -j+1, ..., j-1, j$ associated with the z-projection of the total angular momentum. These new eigenstates are spin orbitals [11, 53]:

$$|nlsjm_j\rangle = \sum_{m_l m_s} |nlsm_l m_s\rangle \langle lsm_l m_s|lsjm_j\rangle\,, \tag{2.15}$$

where $\langle lsm_l m_s|lsjm_j\rangle$ are the Clebsh-Gordan coefficients, which are zero for all $m_l + m_s \neq m_j$. The result of spin-orbit coupling is for magnetic states to become mixed, meaning that orbital and spin angular momentum are no longer conserved quantities but the total angular momentum is. As an example let us construct the spin orbitals of the 2p state of hydrogen:

$$|n, l, s, j, m_j\rangle \tag{2.16}$$

$$|2, 1, 1/2, 1/2, 1/2\rangle = \frac{-1}{\sqrt{3}}|2, 1, 1/2, 0, \alpha\rangle + \sqrt{\frac{2}{3}}|2, 1, 1/2, 1, \beta\rangle\,, \tag{2.17}$$

$$|2, 1, 1/2, 1/2, -1/2\rangle = -\sqrt{\frac{2}{3}}|2, 1, 1/2, -1, \alpha\rangle + \frac{1}{\sqrt{3}}|2, 1, 1/2, 0, \beta\rangle\,, \tag{2.18}$$

$$|2, 1, 1/2, 3/2, 3/2\rangle = |2, 1, 1/2, 1, \alpha\rangle\,, \tag{2.19}$$

$$|2, 1, 1/2, 3/2, -3/2\rangle = |2, 1, 1/2, -1, \beta\rangle\,. \tag{2.20}$$

As we can see, the only difference between the m_j states is the relative weighting of the constituent hydrogenic wavefunctions, with the $|m_j| = 1/2$ states combinations of the hydrogenic wavefunctions with $m_l + m_s = \pm 1/2$. Thus, if we were to measure the z-component of the spin or orbital angular momentum of these states over time, we would find that they fluctuate with only the z-component of the total angular momentum remaining constant. Also notice that the n and l quantum numbers remain the same, so the radial distribution of the charge density remains the same.

2.1.2 Multielectron Wavefunctions

We have now built up the necessary machinery to discuss multi-electron atoms. The next level of complexity to address is multi-electron atoms with non interacting electrons [11]. We can write the non interacting multi-electron Hamiltonian as:

$$\mathcal{H} = \sum_i \frac{-\hbar^2}{2\mu}\boldsymbol{\nabla}_i^2 - \frac{Ze^2}{4\pi\varepsilon_0 r_i}, \tag{2.21}$$

where i runs over all electrons. Thus, a naive description of the helium atom would be

$$\mathcal{H}_{He} = \frac{-\hbar^2}{2\mu}\boldsymbol{\nabla}_1^2 - \frac{Ze^2}{4\pi\varepsilon_0 r_1} + \frac{-\hbar^2}{2\mu}\boldsymbol{\nabla}_2^2 - \frac{Ze^2}{4\pi\varepsilon_0 r_2}. \tag{2.22}$$

There are no cross terms in this Hamiltonian, so the N-electron wavefunction is simply the product of hydrogenic wavefunctions, known as the Hartree Product:

$$\Psi(\mathbf{r}_1, \mathbf{r}_2, ..., \mathbf{r}_N) = u_\alpha(\mathbf{r}_1)u_\beta(\mathbf{r}_2)...u_\omega(\mathbf{r}_N), \tag{2.23}$$

where $\mathbf{r}_i$ are the position coordinates of electron i and the Greek letters represent some unique combination of quantum numbers n, l, m_l, m_s as required by the Pauli exclusion principle. This wavefunction is not anti-symmetric, which is also required by the Pauli exclusion principle. A new entity called the Slater determinant guarantees wavefunction anti-symmetry [11, 30, 89]:

$$\Psi(\mathbf{r}_1, \mathbf{r}_2, ..., \mathbf{r}_N) = \frac{1}{\sqrt{N!}} \begin{vmatrix} u_\alpha(\mathbf{r}_1) & u_\beta(\mathbf{r}_1) & \cdots & u_\omega(\mathbf{r}_1) \\ u_\alpha(\mathbf{r}_2) & u_\beta(\mathbf{r}_2) & \cdots & u_\omega(\mathbf{r}_2) \\ \vdots & \vdots & \ddots & \vdots \\ u_\alpha(\mathbf{r}_N) & u_\beta(\mathbf{r}_N) & \cdots & u_\omega(\mathbf{r}_N) \end{vmatrix}. \tag{2.24}$$

For example the ground state of helium is

$$\Psi(\mathbf{r}_1, \mathbf{r}_2) = \frac{1}{\sqrt{2!}} \begin{vmatrix} u_{1,0,0,\alpha}(\mathbf{r}_1) & u_{1,0,0,\beta}(\mathbf{r}_1) \\ u_{1,0,0,\alpha}(\mathbf{r}_2) & u_{1,0,0,\beta}(\mathbf{r}_2) \end{vmatrix} \tag{2.25}$$

$$= \frac{1}{\sqrt{2}}(u_{1,0,0,\alpha}(\mathbf{r}_1)u_{1,0,0,\beta}(\mathbf{r}_2) - u_{1,0,0,\beta}(\mathbf{r}_1)u_{1,0,0,\alpha}(\mathbf{r}_2)) \tag{2.26}$$

$$= \frac{1}{\sqrt{2}}\psi_{1,0,0}(\mathbf{r}_1)\psi_{1,0,0}(\mathbf{r}_2)(|\alpha\rangle_1 |\beta\rangle_2 - |\beta\rangle_1 |\alpha\rangle_2). \tag{2.27}$$

Notice that the positional wavefunctions, ψ, indicate both electrons are in the 1s state. The spin vectors indicate they are in opposite spin states, but because they are indistinguishable we have an anti-symmetric expansion of spin vectors rather than a Hartree product.

This is as far as we can go analytically. The next step is to introduce electrostatic interactions between electrons into the Hamiltonian [30]:

$$\mathcal{H} = \sum_i \frac{-\hbar^2}{2\mu}\boldsymbol{\nabla}_i^2 - \frac{Ze^2}{4\pi\varepsilon_0 r_i} + \sum_{i>j} \frac{e^2}{4\pi\varepsilon_0 r_{ij}}, \tag{2.28}$$

where r_{ij} is the distance between electrons i and j. The introduction of this electron correlation term makes the solutions of the new Hamiltonian generally non-analytic because it is in the same class of problems as the Newtonian N-body problem. For small atoms like helium and lithium, there are strategies for finding the wavefunctions and eigenenergies, but these methods are not generally applicable to solving the multi-electron Hamiltonian.

The modern strategy for determining these quantities is known as the Hartree-Fock or Self-Consistent Field Approximation. Instead of treating the electron correlation term explicitly, we approximate the effect of Coulomb repulsion as a negative charge distribution that acts to screen the charge of the nucleus. Thus, electron i feels a new potential:

$$U_i(r_i) = \left\langle \sum_{j\neq i} \frac{e^2}{4\pi\varepsilon_0 r_{ij}} \right\rangle, \tag{2.29}$$

where the brackets represent a spherical integral over the wavefunctions for each electron j. Thus, the Hamiltonian is of the form:

$$\mathcal{H} = \sum_i \frac{-\hbar^2}{2\mu}\boldsymbol{\nabla}_i^2 - \frac{Ze^2}{4\pi\varepsilon_0 r_i} + U_i(r_i). \tag{2.30}$$

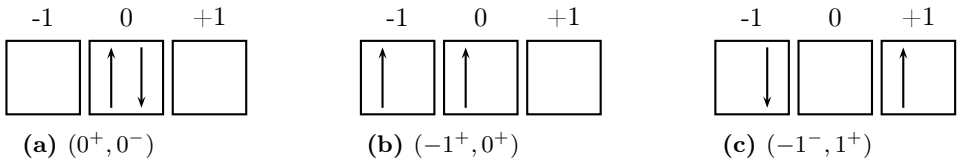

(a) $(0^+, 0^-)$ **(b)** $(-1^+, 0^+)$ **(c)** $(-1^-, 1^+)$

Figure 2.3: Example valence electron states of the [He]$2s^2 2p^2$ electron configuration of carbon.

The wavefunctions of this Hamiltonian can be computed, but because of the integral required to generate the screening potential, the wavefunctions have to be known *a priori*. To rectify this issue, we guess a set of trial wavefunctions then use an iterative method to converge on a reasonable set of solutions. For example, for the ground state of helium we would guess the Slater determinant given in equation 2.25 as our trial wavefunction. Because the Coulomb interaction term screens the nuclear charge, we use the nuclear charge Z as the variational parameter for our optimization [5, 24, 69, 89]. Notice that by only allowing the nuclear charge to vary, the spherical harmonics remain unperturbed; only the radial functions R_{nl} of the solution vary because they depend on Z. We can repeat this process for excited states as well to construct energy level diagrams.

In practice, performing these optimizations is rather difficult, particularly for larger atoms like the rare earths. Research into ways of performing these computations efficiently and accurately is still a rich area, particularly in the computation of heavy atoms and the $U_i(r_i)$ potential [24, 89].

2.1.3 Russell-Saunders and j-j Coupling

Similar to single-electron atoms, we can now include relativistic effects into our multi-electron Hamiltonian. We will introduce spin-orbit coupling by summing over the spin-orbit coupling effects of the individual electrons [41, 42, 53]:

$$\mathcal{H}_{SO} = \sum_i \zeta(r_i) l_i \cdot s_i, \tag{2.31}$$

where i is over all electrons. When spin-orbit coupling is a small perturbation, the total orbital angular momentum $L = \sum_i l_i$ and spin $S = \sum_i s_i$ are approximately good quantum numbers. This is known as Russell-Saunders coupling.

Eigenstates of this system are Slater determinants that include the core electron states and all possible combinations of valence electron m_l and m_s states. For example, carbon has electron configuration [He]$2s^2 2p^2$. We use a shorthand notation for the Slater determinants that represent the microstates of this system:

$$\left|([He]2s^1 2p^2) L S M_L M_S\right\rangle = (m_l^{m_s}, m_l^{m_s}), \tag{2.32}$$

where $L = \sum_i l_i$, $S = \sum_i s_i$, $M_L = \sum_i m_{l,i}$, $M_S = \sum_i m_{s,i}$ and the entries in parentheses represent the specific microstate of the valence electrons in the $2p^2$ electron configuration. Figure 2.3 diagrams several possible microstates of the carbon $2p^2$ valence electrons and their corresponding Slater determinants. Microstates which share L and S quantum numbers are called an L-S term. In spectroscopy, L-S terms are written as

$$^{2S+1}L, \tag{2.33}$$

where $2S+1$ is called the term's multiplicity and L is written as a letter: $S=0$, $P=1$, $D=2$, $F=3$, $G=4$, $H=5$, ... analogous to the notation for angular momentum states of the hydrogenic atom. The [He]$2s^2 2p^2$ configuration of carbon has L-S terms ^1D, ^3P and ^1S. The microstates associated with these L-S terms are given in table 2.1. The method for computing these L-S terms

Table 2.1: The microstates of the carbon and the L-S terms to which they belong.

^{1}S	(0^+,0^-)
^{3}P	(1^+,0^+) (1^-,0^+) (1^-,0^-) (1^-,-1^-) (0^-,-1^-) (0^-,-1^+) (0^+,-1^+) (1^+,-1^+)
^{1}D	(1^+,1^-) (1^+,0^-) (1^+,-1^-)(0^+,-1^-)(-1^+,-1^-)

is given in Tinkham [89].

Finally, analogous to spin-orbit coupling in hydrogen, the total angular momentum $\mathbf{J}=\mathbf{L}+\mathbf{S}$ can be used to diagonalize the Hamiltonian given in equation 2.31. These wavefunctions are generally linear combinations of Slater determinants. Every L-S term, assuming $L\neq 0$, has $2S+1$ J states associated with it, where $J=|L-S|,|L-S|+1,...,L+S$. If $L=0$, the L-S term is associated with only one J state, $J=S$. A Russell-Saunders term symbol specifies values for J:

$$^{2S+1}L_J, \tag{2.34}$$

where every Russell-Saunders term symbol is a set of $2J+1$-fold degenerate Slater determinants with magnetic quantum number M_J. Thus, the ^3P term of carbon contains 3 Russell-Saunders terms: $^3P_2$, $^3P_1$ and $^3P_0$. At this point, it is important to note that a pen-and-paper calculation of these wavefunctions is usually not useful. Due to the effects of spin-orbit coupling, even the states associated with L-S terms tend to be linear combinations of Slater determinants, thus for the most part, the wavefunctions associated with L-S terms and Russell-Saunders terms must be calculated using a self-consistent field approach [89].

When the effects of spin-orbit coupling cannot be treated as small perturbations, which is usually the case for atoms with $Z>40$, we enter a regime called j-j coupling. In this regime, microstates of the system are no longer Slater determinants of $|nlm_l m_s\rangle$ states but of $|nlsjm_j\rangle$ states. In this case, we can still use Russell-Saunders term symbols to label sets of M_J microstates [28, 89].

2.1.4 Crystal Field Effects

There are several more corrections we can add to the multi-electron Hamiltonian [53], like nuclear-spin/electron-spin coupling. We will not be discussing them here, but it is important to note that these other corrections are needed when performing *ab initio* calculations to arrive at wavefunctions and eigenenergies that properly model reality. Instead, we turn our attention to what happens when we no longer consider the free atom, but collections of atoms in a insulating crystal.

There are many approaches to identifying the behavior of an atom in a solid state. For example, in covalently bonded materials, valence electrons spread out into charge density waves over the volume of the crystal. The states of these charge densities are called a band structure, which are usually calculated using Density Functional Theory [103].

In materials containing rare earths on the other hand, the rare earth ions are typically ionically bonded, which means their states can be considered as the free ion states discussed previously but in an effective electric field. We can use this simplification because doubly and triply ionized Lanthanides have electron configuration [Xe]$4f^n$. The $4f^n$ valence electrons of Lanthanide ions are screened from their environment by the $5p^6$ core electrons, preventing them from participating in covalent bonds. The screening of 4f electrons by 5p electrons is demonstrated in figure 2.4, which plots the radial probability density of the 4f and 5p states of hydrogen. This property of rare earth

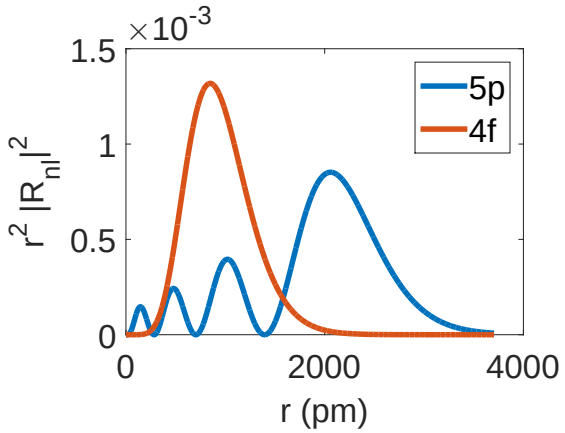

Figure 2.4: A comparison of the radial probability density of the 5p and 4f states of hydrogen.

ions makes them uniquely suited for solid state applications, such as in laser gain media and quantum memories, because they do not interact strongly with their crystallographic environment [45].

The calculation of energy levels of rare earth ions in insulating materials requires that we modify the electrostatic potential felt by the electrons. The simplest model of the crystal field is to assume that it is generated by spherically symmetric point charges at a distance R from the central ion [53]:

$$\mathcal{H}_{\mathrm{CF}} = \frac{1}{4\pi\varepsilon_0} \sum_i \sum_l \frac{Z_l e^2}{|\mathbf{R}_l - \mathbf{r}_i|}, \tag{2.35}$$

where l runs over all ligand ions, and i runs over all electrons in the central ion. The next refinement is to decompose this Hamiltonian into a series of spherical harmonics [53]. Qualitatively, this crystal field acts to lift the 2J+1 degeneracy of the term symbols for the free ion. From group theory considerations and knowledge of the point symmetry of the site that a specific ion occupies, it is possible to calculate the amount of levels any given term splits into without performing a full calculation with the crystal-field Hamiltonian. This approach often has more utility because energy level calculations for rare-earth ions are usually not performed from first principles, but instead are often phenomenological fits to experimental spectra [53]. Thus, to properly determine transition energies, we only need to know the amount of transitions.

Detailed explanations of this process can be found in many books including Dresselhaus et al. [17] and Powell [73]. Group theory tells us that crystal fields of high symmetry only partially lift term degeneracy, and low symmetry fields completely lift the degeneracy. For example, the ${}^4I_{9/2}$ ground state of Nd^{3+} in $Cs_2NaNdCl_6$, a type of elpasolite, is split into three levels due to the highly

symmetric octahedral (O_h in Schönflies notation) crystal field of the surrounding Cl^- ligands [22] (figure 2.5).

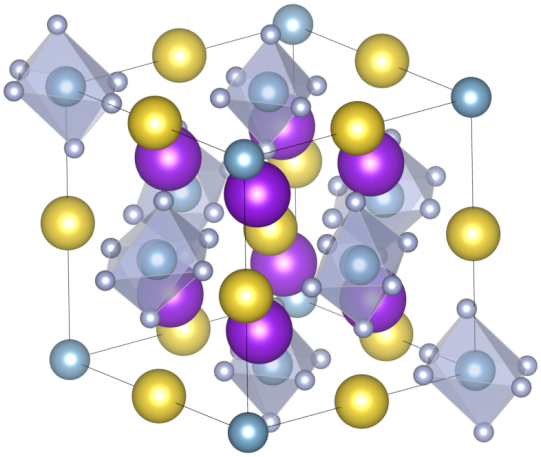

Figure 2.5: A unit cell of elpasolite with anion coordination polyhedra showing the anion octahedral crystal field [63].

An example of a low symmetry environment is Nd^{3+} doped $LiYF_4$, which has four fluorine anions in S_4 symmetry around the neodymium cation [16]. In this system the ten-fold degenerate ground state is split into 5 two-fold degenerate levels. This is because Nd^{3+} has Kramer's degeneracy[1], which can only be lifted with an applied magnetic field [17, 42]. Hence, each level of the ground state is split into distinct M_J states ($\pm 1/2$, $\pm 3/2$, $\pm 5/2$, $\pm 7/2$, $\pm 9/2$) up to Kramer's degeneracy. Group theory can only tell us how many states the terms split into. In order to know how they are ordered, we would have to calculate the wavefunctions and eigenergies of these states using Hartree-Fock or some other variational method.

2.2 Semiconductor Nanoparticles

Well defined energy levels that can be addressed optically are not a property unique to atoms. In semiconductors, discrete energy levels can exist and be engineered when the size of the crystals are on the order of the de Broglie wavelength of the electron in the lattice, which is on the order of 100nm or less. Like atoms, this property makes semiconductor nanoparticles, also known as quantum dots (QDs), similarly useful as probes of their environment.

2.2.1 Quantum Confinement

A complete quantum mechanical model of QDs begins with the usual Hamiltonian terms:

$$\mathcal{H} = \frac{-\hbar^2}{2m^*}\boldsymbol{\nabla}^2 + V, \tag{2.36}$$

[1] An atom is Kramer's degenerate when the total spin S is a half-integer. [45]

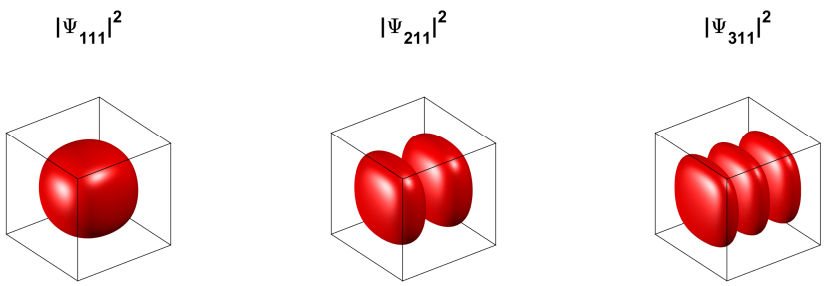

Figure 2.6: Isoclines of the probability density of an electron in a cubic hard wall potential with $n_x = 1, 2, 3$.

where m^* is the electron effective mass and V includes terms for the periodic potential of the lattice ions, Coulomb interactions between electrons and holes, pseudo-particle interactions (like phonons and plasmons) with electrons, and relativistic corrections like spin-orbit coupling. Finding the wavefunctions and eigenenergies of this Hamiltonian generally requires a variational approach similar to the Hartree-Fock method [103].

We can derive the discrete energy level structure of these systems by reducing this Hamiltonian to the hard wall model. In this model the potential V is flat with infinite barriers, thereby removing the effects of the underlying crystal structure and correlation effects. The solutions of this Hamiltonian are particularly important because they usually provide a good ansatz for the envelope functions used to solve the Bloch equations that are a result of including the crystal structure of the lattice into the potential.

The wavefunctions of this equation are the well known 3-D particle in a box solution for rectangular prismatic QDs and particle in a sphere solution for spherical QDs [4]. For a particle in a box these wavefunctions are

$$\Psi_{n_x,n_y,n_z} = \begin{cases} \left(\frac{8}{L_x L_y L_z}\right)^{1/2} \sin\left(\frac{n_x \pi x}{L_x}\right) \sin\left(\frac{n_y \pi y}{L_y}\right) \sin\left(\frac{n_z \pi z}{L_z}\right) \text{ where } (x,y,z) \leq (L_x, L_y, L_z) \\ 0 \text{ otherwise} \end{cases}, \quad (2.37)$$

with eigenenergy:

$$E_{n_x,n_y,n_z} = \frac{\hbar^2 \pi^2}{2m^*} \left(\frac{n_x^2}{L_x^2} + \frac{n_y^2}{L_y^2} + \frac{n_y^2}{L_y^2} \right), \quad (2.38)$$

where L_i is the length of the box in direction i and n_i are quantum numbers. Figure 2.6 provides an example of what the probability density of these solutions looks like.

For a particle in a sphere, the solution is [26]

$$\Psi_{nlm} = \begin{cases} A_{nl}\, j_l(\beta_{nl} r/R) Y_l^m(\theta, \phi) \text{ where } r \leq R \\ 0 \text{ otherwise} \end{cases}, \quad (2.39)$$

where A_{nl} are normalization constants, $j_l(r)$ are lth-order Bessel functions of the first kind, β_{nl} is the nth zero of the lth Bessel function of the first kind, R is the radius of the QD and Y_l^m are the

spherical harmonics. This solution has eigenenergy:

$$E_{nl} = \frac{\hbar^2}{2m^* R^2} \beta_{nl}^2. \tag{2.40}$$

An example of what the probability density of these solutions look like are given in figure 2.7.

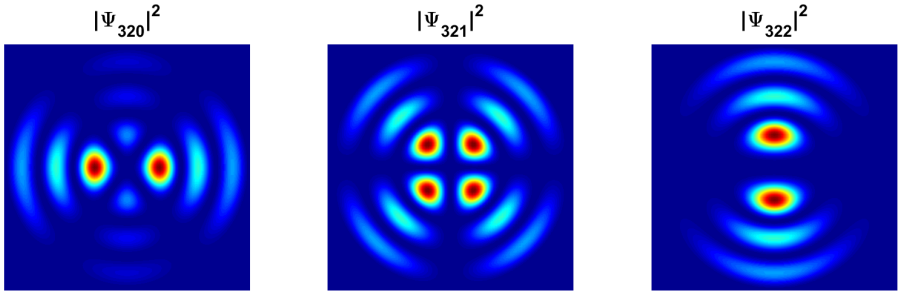

Figure 2.7: False color image of the probability amplitude of the solutions for the spherical hard wall potential with $m = 0, 1, 2$.

Notice that these solutions localize the electrons to the interior of the nanoparticle; this is called quantum confinement. A characteristic feature of 0-dimensional quantum confinement is that all states of the free particles in the system have well defined energies, which are inversely proportional to the size of the QD squared. Thus, smaller QD nanoparticles will have wider energy level spacings than larger ones.

Chapter 3

Dipole Transitions

Due to differences in energy between the states of a system, systems will settle into the lowest energy configuration and remain there. This is the ground state. For a system to occupy states with energy higher than the ground state, it must absorb energy. Energy can come in many flavors, thermal and electromagnetic energy being the two most relevant to spectroscopy. Systems also return to the ground state by emission of these types of energy. To understand how this happens in condensed matter systems, we will first explore the Lorentz Oscillator to develop a classical picture of state transitions. Afterward, we will explore the quantum theory that predicts how transitions between electronic states occur.

3.1 The Lorentz Oscillator Model

Classically, we can picture an atom as a dipole in which the energy levels of the electron lie at varying distances from the nucleus, i.e., the Bohr model. As a result, due to the charge separation, the atom has an electric dipole moment:

$$\mathbf{D} = e\mathbf{r}, \tag{3.1}$$

where e is the fundamental unit of charge and $\mathbf{r}$ is the distance vector that points from the nucleus to the electron. In general, not all states of an atom have dipole moments, but this model is a good starting point for developing a physical intuition about the dipole transition process.

We can model the transitions between states as a mass spring system, where the spring's equilibrium position is the radius of the destination energy level. Excitation is modeled as a driving term, and because we are considering optical absorption, the driving field is sinusoidal. Emission, which occurs simultaneously for a continuously driven system, is modeled as a damping term which couples the electron to the electro-magnetic field as well as the local environment, which is also capable of dissipating energy. We begin our analysis with the damped driven harmonic oscillator:

$$m\frac{\mathrm{d}^2 D}{\mathrm{d}t^2} + \gamma\frac{\mathrm{d}D}{\mathrm{d}t} + kD = -e^2 E_0 \cos(\omega t), \tag{3.2}$$

where D is er and r is the distance of the electron from the nucleus, and the driving term is the electric field of a photon interacting with the atom. The friction term is interpreted as energy lost

by the oscillator to the electro-magnetic field, i.e., photons. The solution to this equation is the real value of

$$\tilde{r}(t) = \frac{-eE_0}{m} \frac{1}{\omega_0^2 - \omega^2 + i\omega\Gamma} e^{i\omega t}, \tag{3.3}$$

where $\omega_0 = \sqrt{k/m}$ is the resonance frequency and $\Gamma = \gamma/m$ [8, 20]. We can compute the spectrum of the emitted radiation by computing the cycle-averaged power of the damping term [45]:

$$< P_{\text{damping}} >= \frac{\omega^2 e^2 E_0^2}{m} \left[\frac{\Gamma/2}{\left(\omega^2 - \omega_0^2\right)^2 + \left(\omega\Gamma\right)^2} \right], \tag{3.4}$$

For radiation in the UV, visible and near infrared, the damping term $\Gamma \ll \omega_0$. Usually ω_0/Γ is on the order of 1000 or more. In this limit, $\omega \approx \omega_0$, thus:

$$< P_{\text{damping}} >\approx \frac{e^2 E_0^2}{4m} \left[\frac{\Gamma/2}{\left(\omega - \omega_0\right)^2 + \left(\Gamma/2\right)^2} \right]. \tag{3.5}$$

The term in brackets is called the Lorentz-Cauchy distribution or, more commonly in spectroscopy, the Lorentzian function. The damping term is the full width at half maximum (FWHM) of the distribution. From this analysis we can see that as damping increases, the linewidth (FWHM) of the transition increases (figure 3.1), which is a key feature of the dipole transition.

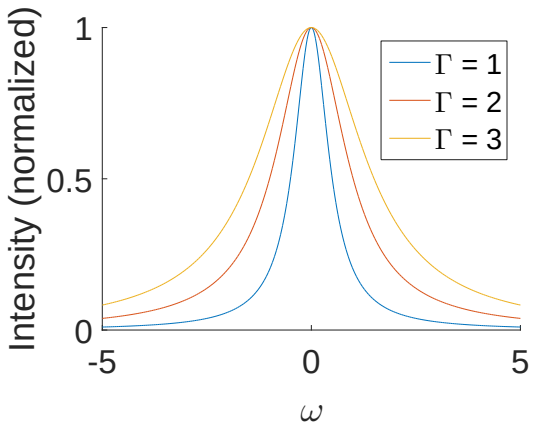

Figure 3.1: The shape of the Lorentzian with changing FWHM.

Furthermore, we can identify the lineshape of the absorption spectrum of the dipole by noting that the energy emitted by the oscillator must also be the energy absorbed. Therefore, the cycle averaged power delivered to the oscillator is simply equation 3.5. We now compute the absorption by dividing the absorbed power by the power (intensity) of the incident photon:

$$\alpha(\omega) =< P_{\text{damping}} > /I_0 \tag{3.6}$$

$$= \frac{1}{1/2E_0^2} \frac{e^2 E_0^2}{4m} \left[\frac{\Gamma/2}{\left(\omega - \omega_0\right)^2 + \left(\Gamma/2\right)^2} \right] \tag{3.7}$$

$$= \frac{e^2}{2m} \left[\frac{\Gamma/2}{\left(\omega - \omega_0\right)^2 + \left(\Gamma/2\right)^2} \right]. \tag{3.8}$$

Thus, the peak of the absorption spectrum occurs at the same frequency as the emission and has the same exact lineshape.

3.2 Dipole Transition: The Quantum Formulation

We now move on to a quantum treatment of electronic transitions. This approach allows us to make predictions about the strength, probability and rate at which transitions between the states of rare earth ions and quantum dots occur for not only dipole but higher order transitions as well. This departs from the Lorentz Model, whose only real predictive power is the spectral shape of dipole transitions. We start by, again, deriving the lineshape of the transitions between two energy levels but this time by solving the full time-dependent Schrödinger equation. The Hamiltonian used to generate the time-dependent states of atoms and QDs satisfies

$$\mathcal{H}_0\Psi = i\hbar\frac{\partial\Psi}{\partial t}, \tag{3.9}$$

where Ψ is now a function of spatial and temporal coordinates and $\mathcal{H}_0$ is the Hamiltonian of the system under consideration. The wavefunction Ψ that satisfies this equation is [2, 30, 92, 101]

$$\Psi = \sum_k c_k(t)\,|k\rangle \exp\left(\frac{-iE_kt}{\hbar}\right), \tag{3.10}$$

where k is the set of quantum numbers that label the eigenstates of $\mathcal{H}_0$, E_k is the eigenenergy of state $|k\rangle$ and $c_k(t)$ is a weighting that satisfies the normalization condition

$$\sum_k |c_k(t)|^2 = 1. \tag{3.11}$$

Next, we introduce a new term to the Hamiltonian that describes the interaction of the photon with the system. We treat this interaction in the single photon limit so it is only a small perturbation [92, 101], in which case Ψ is approximately a valid solution to

$$(\mathcal{H}_0 + \mathcal{H}')\Psi = i\hbar\frac{\partial\Psi}{\partial t}, \tag{3.12}$$

where $\mathcal{H}'$ is the perturbation. This perturbing Hamiltonian can take the form of electric dipole (E1 transition), electric quadrapole (E2 transition), magnetic dipole (M1 transition), and other higher order transitions. In fact, this analysis shows that any of the multipole interactions with light will generate the same lineshape with only their relative intensities and selection rules to distinguish them. After operating equation 3.12 on the state given in equation 3.10 we arrive at

$$\sum_k c_kE_k\,|k\rangle \exp\left(\frac{-iE_kt}{\hbar}\right) + \sum_k c_k\mathcal{H}'\,|k\rangle \exp\left(\frac{-iE_kt}{\hbar}\right) = i\hbar\sum_k \frac{\partial c_k}{\partial t}\,|k\rangle \exp\left(\frac{-iE_kt}{\hbar}\right). \tag{3.13}$$

We now define a state $|f\rangle$ that represents the state being transitioned to. If $E_f > E_k$, the transition is an absorption process, and if $E_f < E_k$, the transition is an emission process. After operating the final state on equation 3.13 from the left the first sum drops out of because $|k\rangle$ and $|f\rangle$ are assumed to be orthogonal:

$$\langle f|\sum_k c_k\mathcal{H}'\,|k\rangle \exp\left(\frac{-iE_kt}{\hbar}\right) = \langle f|\,i\hbar\sum_k \frac{\partial c_k}{\partial t}\,|k\rangle \exp\left(\frac{-iE_kt}{\hbar}\right). \tag{3.14}$$

As a result of the same orthogonality assumption, this equation reduces to

$$\frac{\partial c_f}{\partial t} = \frac{-i}{\hbar}\sum_k c_k\,\langle f|\,\mathcal{H}'\,|k\rangle \exp\left(\frac{i(E_f - E_k)t}{\hbar}\right). \tag{3.15}$$

Let us consider a transition between an initial state $|a\rangle$ and final state $|b\rangle$:

$$\frac{\partial c_b}{\partial t} = \frac{-i}{\hbar} c_a \langle b| \mathcal{H}' |a\rangle \exp\left(\frac{i(E_b - E_a)t}{\hbar}\right). \tag{3.16}$$

For a dipole transition induced by a photon, the perturbation takes the form [11]

$$\mathcal{H}' = e\mathbf{r} \cdot E_0 \hat{\boldsymbol{\varepsilon}} \exp(-i\omega t), \tag{3.17}$$

where $\hat{\boldsymbol{\varepsilon}}$ is the polarization state of the light. Notice that the photon is treated as a classical EM wave, hence this analysis is truly only semi-classical. Equation 3.16 becomes

$$\frac{\partial c_b}{\partial t} = \frac{-i}{\hbar} c_a \langle b| E_0 e(\mathbf{r} \cdot \hat{\boldsymbol{\varepsilon}}) |a\rangle \exp\left(\frac{i(E_b - E_a)t}{\hbar}\right) \exp(-i\omega t). \tag{3.18}$$

Thus, we can see that dipole transitions explicitly couple states for which the off-diagonal matrix element of the dipole operator are non-zero, relative to the incident polarization. We will call this constant D_{ba}, resulting in:

$$\frac{\partial c_b}{\partial t} = \frac{-i}{\hbar} c_a D_{ba} \exp(i(\omega_{ba} - \omega)t). \tag{3.19}$$

It can be shown that if $E_a > E_b$, the coefficient c_a varies as

$$c_a(t) = \exp\left(\frac{-t}{2\tau}\right), \tag{3.20}$$

where τ is the excited state lifetime and also the population excited state lifetime [11, 30]. Inserting equation 3.20 into equation 3.19, we arrive at a partial differential equation for c_b:

$$\frac{\partial c_b}{\partial t} = \frac{-i}{\hbar} D_{ba} \exp\left(-i[\omega - \omega_{ab}]t - \frac{t}{2\tau}\right). \tag{3.21}$$

For static spectroscopy, we are interested in the population measured after a very long time. Thus, we wish to compute $|c_b(\infty)|^2$:

$$|c_b(\infty)|^2 = \left| \int_0^\infty \frac{\partial c_b}{\partial t} \mathrm{d}t \right|^2 \tag{3.22}$$

$$= \left| \frac{-iD_{ba}/\hbar}{(1/2\tau) - i(\omega - \omega_{ab})} \right|^2 \tag{3.23}$$

$$= \frac{D_{ba}/\hbar}{(1/2\tau)^2 + (\omega - \omega_{ab})^2}. \tag{3.24}$$

We have, again, arrived at the Lorentzian distribution. This lineshape will be identical for higher order transitions like quadrapole and octapole transitions because the time dependence of $\mathcal{H}'$ that leads to the Lorentzian shape is the oscillatory portion of the EM wave. The matrix element of these higher order transitions will scale the total area of the transition because they appear in the numerator only. Furthermore, we have also derived a very important property of electronic transitions, in that the linewidth of the emission or absorption spectrum Γ is equal to the inverse of the population lifetime. This quantity is called the homogeneous linewidth of the transition.

$$\Gamma = \frac{1}{\tau} \tag{3.25}$$

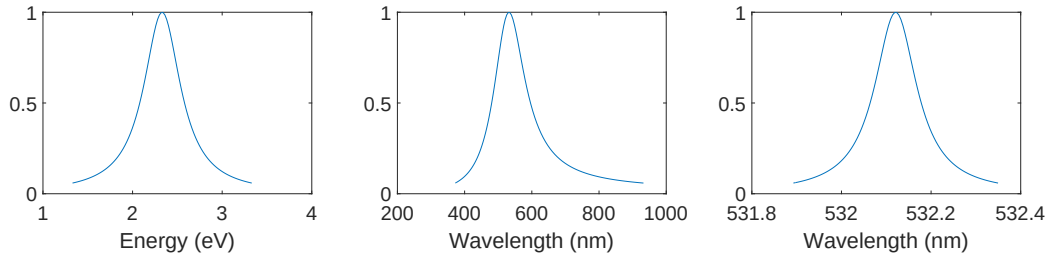

Figure 3.2: Sample Lorentzian distributions plotted with (a,b) $\Gamma = 0.5\,\text{eV}$ and (c) $\Gamma = 0.0005\,\text{eV}$

3.3 Lineshape Measurements

When measuring the emission or absorption spectra of systems, it is important to keep in mind the units used. Notice that equation 3.24 was derived from an analysis of the energy of the system. This means that the lineshape is Lorentzian when plotted as a function of energy or units proportional to energy:

$$E = hf = pc, \tag{3.26}$$

where $\omega = 2\pi f$, h is Plank's constant, p is momentum and c is the speed of light in a vacuum. Thus, plotted as a function of frequency or momentum, the previously derived lineshape will be Lorentzian. Typically, electron-volts are used for near-UV (UV) and visible (VIS) spectroscopy.

Using units proportional to energy can be at odds with the preferred units for measurement devices like Czerny-Turner spectrometers and other dispersive measurement devices, whose behavior is modeled as a function of wavelength. Wavelength is inversely proportional to energy:

$$E = h\frac{c}{\lambda} = pc, \tag{3.27}$$

where λ is wavelength, which is typically measured in nanomaters for UV-VIS-Near IR (NIR). Thus, when measured and plotted in these units, the spectrum of the transition can be heavily skewed. Figures 3.2a and 3.2b are of the same Lorentzian plotted with a much larger width than would be measured in most systems to exaggerate the skewing resulting from plotting the spectrum in units of wavelength. Normal transitions are not so wide. In the limit that $\Gamma \ll \omega_{ab}$, it can be reasonable to plot the spectrum in units of wavelength, which is demonstrated in figure 3.2c. But, for precise measurements of linewidth and center energy, it is important to first convert the wavelength axis of a spectrum to a quantity proportional to energy before performing any analysis.

For VIS-NIR spectroscopy, the most convenient quantity to use for the wavelength axis is spectroscopic wavenumber, usually in units of cm^{-1} (per cm) and defined as

$$\nu \equiv \frac{1}{\lambda}. \tag{3.28}$$

These units are convenient because not only are they directly proportional to energy

$$E = ch\nu, \tag{3.29}$$

but in the VIS-NIR regime the wavenumber axis is on the order of 10,000 per cm, which means linewidths are usually in the range of 0.0001 to 1 per cm. This makes these units computationally convenient when using a computer restricted to performing double precision arithmetic because

rounding errors due to the finite precision of double precision computations are minimized. Alternatively, the same computational benefits can be achieved by picking a good prefix for units proportional to energy, e.g., µeV. Per cm is the standard unit for VIS-NIR spectroscopy. For low energy spectroscopy tera- and giga-Hertz are typically used, and for higher energy spectroscopy electron-volts and milli-electron-volts are standard.

It is also important to remember that to properly relate the Lorentzian linewidth to the excited state lifetime, the Lorentzian width needs to be converted to units of angular frequency. When spectra are analyzed in wavenumbers the excited state lifetime is related to the linewidth by

$$\Delta\nu = \frac{\Gamma}{2\pi c} = \frac{1}{2\pi c\tau}. \tag{3.30}$$

3.4 Line Broadening and Shifting Mechanisms

We can now turn our attention to how interactions between ensembles of ions or QDs and the environment in which they are implanted manifest spectroscopically. We will first discuss interactions that cause spectroscopic line broadening and shifting, which can be used to quantify the effects of interactions that cause dephasing of quantum states, as well as statistical effects like the distribution of stress and strain in crystal. We will then discuss the effects common to rare earth doped insulators and ensembles of QDs, an understanding of which is necessary in order to remove their spectroscopic signatures from measurements on these systems. Doing so allows us to detect the signatures of novel behaviors, like the interaction of trivalent neodymium with a fluctuating magnetic lattice, which we will discuss in Chapter 6.

3.4.1 Phonon-Ion Interactions

Homogeneous broadening, also called lifetime broadening or optical dephasing, occurs when the Lorentzian linewidth of a transition is broadened due to interactions that result in an increased decay rate from an excited state to a lower energy state. These interactions will always cause broadening because the natural lifetime of the isolated particle is always the narrowest a transition spectrum can be.

Ions in a crystal at finite temperature are subject to the phonon bath of that crystal. Furthermore, transitions between electronic states are affected by phonon scattering off these particles as well as phonons emitted or absorbed by these particles during the transition process. In many systems, these interactions heavily modify optical spectra, particularly in transition metals where the 3d valence electrons strongly interact with the crystal lattice. In fact, this is what causes the titanium (III) spectrum in Ti:Sapphire to be so broad, allowing for a tunable laser spectrum over a spectral range of 700 nm to 1 µm [45].

For rare earth ions, due to the screening of the 4f valence electrons by the 5p core electrons, phonon-ion interactions are not a strong effect in the system. Thus, these effects lead to dephasing of the excited states [33] without the generation of vibronic energy levels that result from the strong coupling of atomic energy levels and the continuum of phonon states, i.e., their spectra remain Lorentzian.

In the theory of phonon-ion interactions, the phonon-ion interaction Hamiltonian appears as a series over single phonon, double phonon, etc. interactions. The dominant contribution to linebroadening in rare earth doped materials is the Raman two-phonon scattering process. This interaction describes when a phonon of some energy is absorbed by an ion in an excited state that sends the ion into a virtual state. This state quickly decays via the emission of a phonon of higher energy than the incident phonon and radiative decay of the ion into a lower energy state. This process causes both lineshifting and linebroadening. As a function of temperature, the linebroadening ($\Delta\Gamma$) takes the form

$$\Delta\Gamma = \frac{k_B T_D}{4\pi^2 c\hbar}\int_0^1 \ln\left\{1 + 9\pi^2 W^2 x^6\left[\frac{e^{(xT_D)/T}}{(e^{(xT_D)/T}-1)^2}\right]\times\left[g(x)^2 + W^2\frac{9\pi^2}{4}x^6\right]^{-1}\right\}\mathrm{d}x, \tag{3.31}$$

where k_B is Boltzmann's Constant, T_D is the Debye Temperature of the crystal, W is the dimensionless quadratic coupling constant where $-1 < W \leq \infty$ and $g(x)$ is

$$g(x) = 1 + W\left(1 + 3x^2 + \frac{3}{2}x^3\ln\left\{\frac{1-x}{1+x}\right\}\right). \tag{3.32}$$

$\Delta\Gamma$ will have units of the wavenumber if $\hbar$ is in units of eV s, k_B is in units of $\mathrm{eV\,K^{-1}}$ and c is in units of $\mathrm{cm\,s^{-1}}$, resulting a prefactor of

$$\frac{k_B}{4\pi^2 c\hbar} = 0.110\,618\,22\ /\mathrm{cmK}. \tag{3.33}$$

The temperature dependence of the energy shift ($\Delta\nu$) is

$$\Delta\nu = \frac{k_B T_D}{4\pi^2 c\hbar}\int_0^1 \arctan\left\{\frac{3\pi W x^3 g(x)}{(e^{(xT_D)/T}-1)}\times\left[g(x)^2 + \coth\left(\frac{xT_D}{2T}\right)W^2\frac{9\pi^2}{4}x^6\right]^{-1}\right\}\mathrm{d}x, \tag{3.34}$$

where this is again calculated in units of wavenumber if using the constant given in equation 3.33. It is important to note that these equations assume the Debye approximation holds for the crystal under consideration. If the phonon density of states departs from the Debye approximation substantially, these equations are invalid. To modify them, a more general form of these equations from Hsu and Skinner's seminal papers on Optical Dephasing of Rare Earth Ions [33, 34, 35, 36, 37] can be used.

For most rare earth doped crystals, W is close to zero and is rarely larger than 0.1. This is known as the weak coupling limit. When $T \ll T_D$, these equations can be approximated as:

$$\Delta\Gamma = \frac{9W^2 k_B T_D}{4\hbar c}\left(\frac{T}{T_D}\right)^7\int_0^{T_D/T}\frac{x^6 e^x}{(e^x-1)^2}\mathrm{d}x \tag{3.35}$$

$$\Delta\nu = \frac{3W k_B T_D}{4\pi\hbar c}\left(\frac{T}{T_D}\right)^4\int_0^{T_D/T}\frac{x^3}{(e^x-1)}\mathrm{d}x, \tag{3.36}$$

which are the forms most typically used in the literature [53, 59, 93, 97]. From these forms, we can see that the linebroadening will always increase regardless of the sign on W, but negative values of W result in red shifting of the spectrum and positive values result in blue shifting as a function of increasing temperature. Positive values of W on the order of 0.1 are seen for many transitions in rare earth doped systems. This is the case for neodymium-doped yttrium aluminum garnet [50] and europium-doped yttrium aluminum perovskite [72].

3.4.2 Inhomogeneous Broadening

Inhomogeneous broadening results from the ensemble of optically active species in a system experiencing an environment which imparts some random, non uniform shifting of energy levels. The result is that the lineshape function of the unbroadened ensemble is convolved with the statistical distribution of the environment.

Crystal Strain

In an ideal crystal, the translational symmetry of the atomic arrangement repeats without defects throughout the volume of the crystal. Under these circumstances, every atom will experience identical crystal fields to every other atom occupying the same Wyckoff position within a unit cell. This level of purity is rarely achieved in crystals with any substantial size.

In most crystals we find that, instead, there exist various imperfections. Examples include [64]:

- Dislocations: where lattice planes are deformed within the lattice;
- Vacancies: where atoms are missing within the lattice;
- Anti-site Defects: where, in polyatomic crystals, an atom of one kind substitutes for an atom of a different kind at a specific point in the lattice;
- Charge Traps: Places where charges accumulate, usually as a result of the previously mentioned defects.

These defects not only affect the local crystal field symmetry of any atoms located in the defect region but also warp the crystal, causing stress and strain elsewhere in the crystal. These stresses warp the local crystal field around atoms which would otherwise experience the crystal field associated with a perfect crystal. Physically, this means that any atom in the ensemble experiences a random amount of stark shifting due to random distortions in the crystal field. The way the crystal field around the optically active atom warps is random and in most cases is drawn from the normal distribution. In optical measurements of a statistically large ensemble, this results in the lineshape function of the isolated atom's transition being convolved with a Gaussian [3, 59, 88]:

$$f(\nu) = \int_{-\infty}^{\infty} G(\nu')g(\nu - \nu')\mathrm{d}\nu'. \tag{3.37}$$

Here $g(\nu)$ is the lineshape function of the atomic transition and $G(\nu)$ is the Gaussian distribution. When the transition of interest is a dipole transition, $g(\nu)$ is the Lorentzian distribution. Convolved with a Gaussian, the resulting function is the Voigt distribution.

In the normal course of data analysis, it is computationally inefficient to compute the Voigt distribution via the convolution integral. Instead, we can use an alternative formulation that is computationally faster and more accurate:

$$V(\nu; \nu_0, \Gamma, \sigma, A) = A\frac{\mathrm{Re}[w(z)]}{\sigma\sqrt{2\pi}} \tag{3.38a}$$

$$z = \frac{(\nu - \nu_0) + 2i\Gamma}{\sigma\sqrt{2}}, \tag{3.38b}$$

where $w(z)$ is the Faddeeva function, ν_0 is the center wavenumber, Γ is the Lorentzian full width at half maximum, σ is the Gaussian standard deviation and A is the total area of the distribution [39]. It is important to note that when $\Gamma \to 0$, the line function approaches a pure Gaussian, and when $\sigma \to 0$, the function approaches the Lorentzian distribution of the dipole transition as expected. The amount of inhomogeneous broadening is quantified by the Gaussian full width at half maximum:

$$\Upsilon \equiv 2\sigma\sqrt{2\ln(2)}. \tag{3.39}$$

Size Distribution

In systems with quantum confinement, like semiconductor quantum dots, the energy levels of the system are proportional to the dimensions of the system, e.g., the radius of a spherical nanoparticle (equation 2.40). When an ensemble of these systems are grown, whether chemically or through epitaxy, any member of the ensemble will have a slightly different geometry relative to the average. Thus, like an atom in a crystal lattice, the usual lineshape of the energy level transitions will be convolved with the statistical distribution from which the size of the quantum dots are drawn. Conveniently, the size of nanoparticles tends to be normally distributed, so the ensemble emission from semiconductor nanoparticles can be also be modeled as a Voigt distribution. Furthermore, the inhomogeneous broadening of the ensemble is usually much wider than the homogeneous linewidth. In this limit, the emission from an ensemble of QDs can usually be approximated as a Gaussian or in some cases the log-normal distribution (Appendix A) [10, 27]. The Gaussian, Lorentzian and Voigt distributions are not the only functional forms observed in spectroscopy. There are several other lineshape functions that are commonly used, which are given in Appendix A.

3.4.3 Förster Resonant Energy Transfer

When measuring an inhomogeneously broadened sample, it is possible for subsets of the emitting population to transfer energy between each other. This usually results in a redshifting of the ensemble emission, because the high energy emitters transfer their energy to low energy emitters. One mechanism for energy transfer is Förster Resonant Energy Transfer, typically referred to as FRET[1].

In the photo-physics of fluorophores and quantum dots, electric dipole-dipole interactions are a particularly important mechanism. Due to its distance dependence, FRET is used as a high resolution ruler to overcome optical limits in systems that are far too small to view photographically. Examples include investigations of protein folding [65, 74] and cell membrane composition [46].

Förster Resonant Energy Transfer (FRET) Theory

To understand this process, first consider that the electronic states of a system can process a dipole moment like we saw in Chapter 3. If we have two systems with dipole moments in close proximity, their interaction will affect the energy of the system, and therefore the Hamiltonian. We

[1]Sometimes (typically in biology literature) this mechanism is called Fluorescent Resonant Energy Transfer, this is a misnomer but it is one readers should be aware of due to its popularity.

can see this by first identifying the electric potential generated by a dipole:

$$\Phi = \frac{\mathbf{D} \cdot \mathbf{r}}{4\pi\varepsilon_0 r^3}, \tag{3.40}$$

where $\mathbf{D}$ is the dipole moment defined in equation 3.1, $\mathbf{r}$ is the distance vector between some point in space and the center of the dipole and r is the magnitude of $\mathbf{r}$. The electric field generated by this potential is

$$\mathbf{E} = -\boldsymbol{\nabla}\Phi = \frac{1}{4\pi\varepsilon_0}\left[\frac{3\mathbf{D}\cdot\mathbf{r}}{r^5}\mathbf{r} - \frac{\mathbf{D}}{r^3}\right]. \tag{3.41}$$

The potential energy of a second dipole in this field is

$$V = -\mathbf{E}_1 \cdot \mathbf{D}_2 = \frac{1}{4\pi\varepsilon_0}\left[\frac{3(\mathbf{D}_1\cdot\mathbf{r})(\mathbf{D}_2\cdot\mathbf{r})}{r^5} - \frac{\mathbf{D}_1\cdot\mathbf{D}_2}{r^3}\right], \tag{3.42}$$

where subscripts 1 and 2 label each dipole and r is now the distance between the center of these two dipoles. From this we can see that this mechanism is Coulombic and not mediated by photons. This is, therefore, not an emission/absorption process, which is a common misconception about how this process works.

We next construct a system that includes the Hamiltonians of the individual fluorophores and the dipole-dipole interaction Hamiltonian. The dipole coupling Hamiltonian is treated as a perturbation so that the vacuum states of the uncoupled system are approximately good wavefunctions:

$$\Psi = |d\rangle\,|a\rangle\,, \tag{3.43}$$

where d denotes the wavefunction of the donor fluorophore and a the acceptor. These wavefunctions are treated generally in this derivation so the two coupled systems do not have to be identical; they can be atoms, QDs, fluorescent molecules or any combination of these systems. The important property that needs to be satisfied is that the transition between the ground and excited states of these systems is dipolar.

Under the assumption that nuclear motion is slow relative to the energy transfer process (Born-Oppenheimer Approximation) and that vibronic transitions are more likely to occur between electronic states with significantly overlapping vibrational wavefunctions (Frank-Condon Principle), we find that the energy transfer rate is

$$W_{\mathrm{FRET}} = \frac{\langle\kappa^2\rangle}{\hbar^2 r^6}|D_{dd*}|^2|D_{aa*}|^2\int_{-\infty}^{+\infty}\sigma_{\mathrm{abs.}}^{(a)}\sigma_{\mathrm{fluor.}}^{(d)}\mathrm{d}\omega, \tag{3.44}$$

where W is the transfer rate of the FRET process, $\langle\kappa^2\rangle$ quantifies the relative orientation between the dipoles, D_{dd*} is the matrix element of the dipole operator between the ground and excited states of the donor or acceptor, and the integral quantifies the overlap of the absorption spectrum of the acceptor with the emission spectrum of the donor [62, 76, 90, 92]. From here we can see several important conditions that need to be satisfied:

1. The transitions experienced by the donor and acceptor must be dipolar (by construction).
2. There must be some, but not necessarily complete, overlap of the absorption and emission spectra of the fluorophors involved.

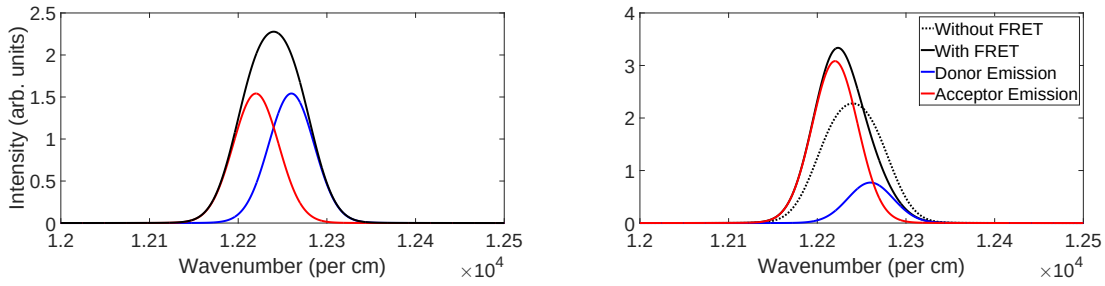

(a) **(b)**

Figure 3.3: (a) An example of emission from an ensemble of QDs with no intra-ensemble FRET. The measured emission (black line) is the sum of donor and acceptor emission. (b) Measured emission from the same ensemble with 50% energy transfer due to FRET. The dotted curve is the emission with no FRET.

3. The process is strongly distance dependent $(1/r^6)$, so the dipoles must be in close proximity.

It is this last property that makes FRET particularly useful as a mechanism for measuring distances between objects that can be tagged by fluorescent species capable of this type of energy transfer. Note that because this distance dependence drops off so quickly, the distance between any two fluorophores is usually no more than 10 nm before the FRET transfer rate is longer than the normal radiative decay rate [92]. Thus, this effect is usually limited to measuring configuration dynamics on the single nanometer length scale.

Experimental Signatures

When measuring an ensemble of QDs with a distribution of sizes, it is likely that the absorption spectrum of the largest dots, those with low transition energies, will overlap the emission spectrum of the smallest dots, those with high transition energies, due to stokes shift[2]. Thus, when the emission spectrum of the ensemble is measured, it will appear distorted from its normal distribution (usually Voigt) due to the higher energy emitters losing their energy to the lower energy emitters. The most basic signature of this is the peak of the emission spectrum of the ensemble is red shifted relative to its emission spectrum without FRET. To understand why, it is useful to treat this data as being generated by two distributions of emitters: donors and acceptors. These individual populations will then have their own separate lineshapes, usually Voigt, that are then added together to generate the measured spectrum (figure 3.3a). When FRET is occurring between the donors and acceptors, the intensity of the donor emission will decrease, resulting in the redshifting of the summed-spectrum peak (figure 3.3b). Furthermore, by comparing the total area of these two distributions, we have a qualitative measure of the intra-ensemble FRET.

An alternate approach is to take time-resolved spectroscopic data. The FRET efficiency, a measure of how probable a donor is likely to decay to its ground state via FRET as opposed to some other mechanism, can be computed by

$$\epsilon = 1 - \frac{\tau_{\text{FRET}}}{\tau_0}, \tag{3.45}$$

[2]Stokes shift is when the peak of the absorption spectrum is shifted to a higher energy than the emission spectrum as a result of vibrational coupling of the energy levels in the fluorophore to its electronic levels.

where $\tau_{\text{FRET}} = W_{\text{FRET}}^{-1}$ is the lifetime of the FRET process and τ_0 is the radiative lifetime plus the lifetimes of all other processes added inversely. Take for example

$$\frac{1}{\tau_0} = \frac{1}{\tau_{\text{radiative}}} + \frac{1}{\tau_{\text{raman}}} + ..., \tag{3.46}$$

where τ_{raman} would be the decay time resulting from a Raman-type decay process. To measure this, one would use a filter to exclude as much of the acceptor emission as possible, then collect time-resolved intensity traces with a single photon counter or streak camera. Because the decay is exponential, the traces can be analyzed by fitting a weighted sum of exponential decays. If there are only two energy transfer processes, the correct model would be

$$I(t) = I_1 \exp\left(\frac{-t}{\tau_1}\right) + I_2 \exp\left(\frac{-t}{\tau_2}\right) + ... + I_n \exp\left(\frac{-t}{\tau_n}\right), \tag{3.47}$$

where $I(t)$ represents intensity as a function of time, I_n is the initial intensity of the n-th decay mechanism, and τ_n is the lifetime of the n-th decay mechanism. Because FRET is a much faster process (on the order of 100s of ps) than normal radiative decay (nanoseconds to microseconds), it is usually trivial to disambiguate which exponential is fitting the FRET decay and which is the normal radiative decay.

Chapter 4

Spectroscopy and Microscopy Methods

Spectroscopy is concerned with measuring the colors absorbed, emitted and scattered by a system. The measurement of light has been one of the most important experimental tools for understanding the properties of physical systems. From Newton and the solar spectrum [68] to Bunsen and the spectrum of combusted molecules [9, 48], the study of light emitted by systems has been used to deduce their fundamental components for nearly 400 years. The dynamics of many systems in nature can be reduced to electrodynamics and energy transfer into an electromagnetic form. Hence, many systems can be explored using electromagnetism and excitations of the electromagnetic field, i.e., light.

In this chapter we will discuss the optical apparatus used in the studies presented in the last two chapters. We will discuss these devices in general, their uses, principles of operation and some experimental considerations when constructing them. Experiment specific details, for example the specific lasers and spectrometers used in the presented work, will be explained during the discussions of the experimental results presented in later chapters.

4.1 Fluorescence Spectroscopy

The collection and quantification of light emitted by a system experiencing a dipole transition is called fluorescence spectroscopy. There are many ways to perform fluorescence spectroscopy. For example, some systems emit light when a solution is created, which is the principle of operation of glow sticks. This is called chemiluminescence. For the systems we have discussed (rare earth ions and quantum dots), luminescence is generated when these systems absorb energy in the form of light (fluorescence), though plasmons, phonons and other forms of energy can also generate luminescence. When these systems inevitably return to a low energy state, they often emit light to release the excess energy. This is fluorescence, and fluorescence carries a lot of information. An experimental analysis of fluorescence gives us information about the energy levels of a system as discussed in Chapter 2 and system interactions and energy transfer mechanisms as discussed in Chapter 3.

To perform fluorescence spectroscopy, one requires a light source and a light detector. The modern fluorescence microscope uses a laser tuned to the energy difference between the energy levels of interest or a laser of such high energy that it excites a system far above the energy levels of interest such that it eventually decays through those levels. For example, in the study of neodymium-doped gadolinium gallium garnet, we use a laser tuned to 808 nm so that the Nd ions enter their second excited state, which then decays into the first excited state, which is the energy level of interest for the neodymium-doped gadolinium gallium garnet study.

To collect the light, we use a spectrometer. A spectrometer is a device that separates light into its constituent colors and records the intensity of each color. The most widely used method is to use a diffraction grating or prism to separate the colors spatially. This spatially separated distribution of colors is recorded with a camera, which allows this method to take advantage of multiplexed collection.

Alternatively, a cavity can also be used. When using a cavity like a Fabry-Perot etalon, one utilizes a photodiode to collect intensity information as a function of cavity length. This information is then Fourier transformed to arrive at spectroscopic information. This method is typically higher resolution than the dispersive method, but acquisition times are often longer.

The most basic fluorescence microscope consists of a laser focused by a lens onto the sample being measured. The focal length and aperture of the lens is chosen taking into consideration the Abbe diffraction limit:

$$d = \frac{\lambda}{2n\sin(\theta)}, \tag{4.1}$$

where d is the size of the smallest resolvable feature, λ is the wavelength of the excitation, n is the index of refraction of the medium the light is being focused through (which is typically 1 for air and thin samples) and θ is the half-angle of the light cone formed by focusing the laser [65, 81]. $n\sin(\theta)$ is also called the numerical aperture (NA) of the focusing lens:

$$NA = n\sin(\theta) = n\sin\left(\arctan\left(\frac{D}{2f}\right)\right) \approx \frac{nD}{2f}, \tag{4.2}$$

where f is the focal length of the lens and D is its diameter. Thus, the smallest resolvable feature (as well as the smallest focused spot) is achieved with a low focal length and a large effective aperture (the circular area the laser fills on back of the lens). For visible spectroscopy, the diffraction limit is typically around $d = \lambda/2.8$, thus green excitation ($500\,\text{nm} - 550\,\text{nm}$) can achieve spatial resolution on the order of 250 nm. This limit is important to consider when averaging over many fluorescent species. When attempting to measure a very dilute sample, it may be necessary to lower the spatial resolution to create the largest focus spot possible, rather than the smallest.

There are typically three different collection geometries:

1. Reflection Geometry: the excitation lens is used for collection (figure 4.1b);
2. Transmission Geometry: a lens conjugate to the excitation lens is used to collimate the fluorescence on the opposite side of the sample (figure 4.1a);
3. Oblique Geometry: a second lens is placed at a particular angle relative to the excitation lens, which is used to collimate the fluorescence.

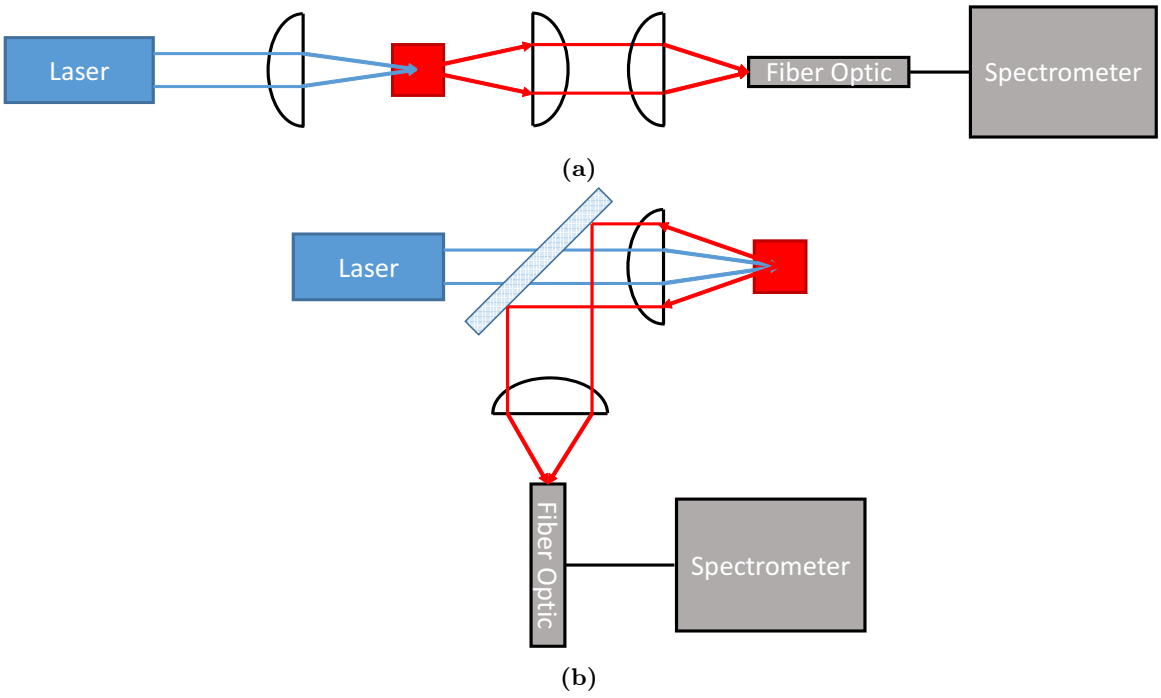

Figure 4.1: (a) Fluorescence microscope in transmission geometry: lenses are black; the sample is the red square; excitation light is blue rays; and fluorescence is depicted as red rays. (b) Fluorescence microscope in reflection geometry: the optical element depicted with blue and white crosshatching is a partially reflective mirror.

Each of these geometries is important and has its own use cases. In the studies presented in this thesis, we use reflection geometry for the QD-Plasmon study and transmission geometry for the neodymium-doped gadolinium gallium garnet study. The collection lens is also chosen considering the diffraction limit, but using the fluorescence wavelength as opposed to the excitation wavelength. After being collected, the light is focused into a spectrometer for analysis. Finally, the intensity of the emitted light is plotted as a function of wavelength or wavenumber. Once recorded, it is possible to use the theory discussed in the previous chapters to model and analyze the spectrum.

4.2 Absorption Spectroscopy

Absorption spectroscopy is a technique for measuring the energy dissipation mechanisms in a system, for example, the energy absorbed by an atom to send it to an excited state. Measuring the absorption of a system requires a tuneable excitation source and a photo-detector. There are several ways to generate an absorption spectrum. The simplest and most widely used method is to excite the sample with a lamp with a broad emission spectrum and collect the light transmitted through the sample with a spectrometer using the setup diagrammed in figure 4.1a. This method has several benefits:

1. Multiplexed collection and excitation result in very fast data acquisition times.

2. Lamps are incoherent sources, so the effects of time- and polarization- dependent processes within a sample are averaged out.

3. This kind of absorption spectrometer can be comparatively inexpensive to purchase or build.

Drawbacks to this method include loss of polarization and temporal information (it's both a drawback and a benefit depending on the information one is trying to gather about a system) and spectral resolution is limited to a few tenths of nanometers when using the average spectrometer.

More advanced absorption spectrometers can be built using tunable lasers or combinations of tunable lasers and lamps, which are useful for studying nonlinear optical processes; pulsed lasers, which are useful for measuring ultra-fast absorption processes (transient absorption spectroscopy); and optical cavities like a Fabry-Perot cavity for constructing ultra-high resolution spectra. The primary benefit lost when attempting to increase temporal or spectral resolution is multiplexed collection, which can cause absorption measurements to have increased acquisition times.

After the excitation passes through the sample, its spectrum is measured, as opposed to the spectrum of light generated by the sample in the case of a fluorescence measurement. This transmission spectrum is then compared to the excitation spectrum without the sample present. The absorption spectrum is generated by computing

$$\alpha(\nu) = 1 - \frac{\mathrm{S}_{trans}(\nu)}{\mathrm{S}_0(\nu)}, \tag{4.3}$$

where S_{trans} is the excitation spectrum transmitted through the sample and S_0 is the excitation spectrum without the samples present, typically called the reference spectrum. Often, this spectrum is presented in units of optical density, which is computed by taking the natural logarithm of the absorptivity:

$$\mathrm{OD}(\nu) = \log(1 - \alpha(\nu)). \tag{4.4}$$

The optical density is in fact dimensionless. This quantity is usually reported because the absorption of a solution containing an absorbing species is proportional to the exponential of the concentration of the species via Beer's Law:

$$\frac{\mathrm{S}_{trans}(\nu)}{\mathrm{S}_0(\nu)} = \exp(\sigma c l), \tag{4.5}$$

where σ is called the absorption coefficient, c is the fluorophore concentration, and l is the optical path length in the sample [18]. Thus, absorption plotted as optical density is a direct way to measure changes in concentration when that quantity is of interest.

4.3 Time Correlated Single Photon Counting

As we discovered in Chapter 3, the excited state of systems which decay via dipole transitions has an excited state probability that decays exponentially (equation 3.20). Thus, the time at which any given emitter decays is random, but the distribution from which these events are sampled is well known. Time Correlated Single Photon Counting (TCSPC) is a technique for measuring this distribution [94].

To perform TCSPC, a pulsed laser with pulses narrower than the lifetime of the decay is used to excite a fluorophore. At some time, this fluorophore emits a photon that is collected by a detector capable of detecting single photons, like an avalanche photodiode or a photomultiplier tube. Timing electronics then bin the time at which this photon was detected. This process is repeated until

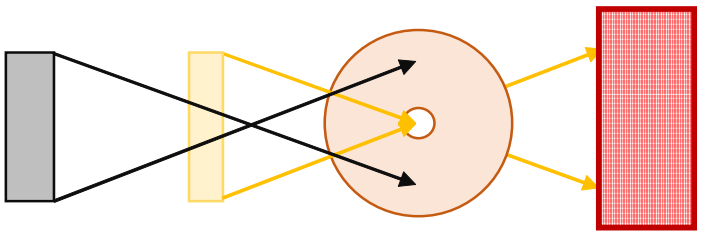

Figure 4.2: A diagram of the spatial filtering used to achieve focal plane selectivity for a confocal microscope. The solid rectangles represent the image of different focal planes which that rays which are focused onto a circular aperture. Only the plane at the correct distance from the pin hole focuses on the pin hole and passes through it, where it is collected by a detector (stripes).

a histogram of detection times is constructed. Assuming the population measured is composed of approximately identical emitters, the time resolved trace corresponds to the excited state probability distribution.

This technique falls under the category of ultra-fast spectroscopy methods. By placing the photodetector in place of a camera in a spectrometer, it is possible to collect time resolved traces as a function of wavelength using the fluorescence setups described in the first section. By having the ability to collect transient information, one loses the multiplexing ability of the camera. This often is not an issue because it is rarely necessary to collect time resolved traces at the spectral resolution of the spectrometer. Usually, one only needs to sample several wavelengths within an inhomogeneously broadened distribution to collect enough information to draw conclusions.

An advanced technique for spectrally multiplexed TCSPC does exist. This technique requires a streak camera to be placed behind a monochromator or some other dispersive element. Time resolved traces are recorded by the camera from which it is possible to calculate photon arrival times for each wavelength simultaneously. The photon arrival times as a function of wavelength are then binned in software, which generates the TCSPC traces. The details of this technique can be found in Becker [7]. The downside to this method is primarily cost. Single point detector TCSPC hardware can be purchased for several thousand dollars at the time of this publication, whereas streak cameras typically cost hundreds of thousands of dollars and are typically more fragile. Though, where high resolution spectrally resolved TCPSPC is required, the acquisition time gains from multiplexing with this technique are likely worth the cost.

4.4 Confocal Microscopy

The ubiquitous method for collecting micrographs of mesoscopic systems is to use a standard light field microscope. A light field microscope image contains information from nearly all focal planes within a sample, which results in degraded image quality because these sample planes are out of focus. They appear blurry and superimposed over the focal plane of interest. This effect can be mitigated by focusing the image of the sample onto a pinhole, which is usually several microns in diameter, before it enters the photodetector. This pinhole acts as a filter (figure 4.2) to reject light from the out-of-focus planes.

The downside to this technique is that a complete image cannot be collected in one exposure. Because of the pinhole, the sample is measured one point at a time. Thus, confocal microscopes not

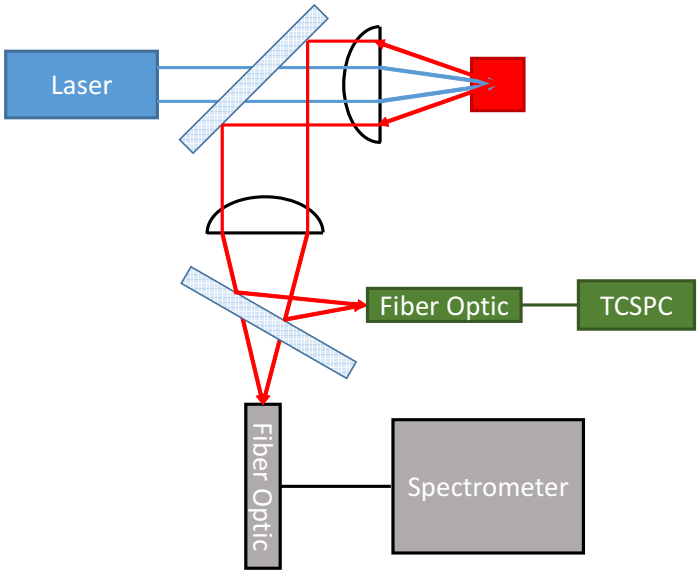

Figure 4.3: A scanning confocal microscope with simultaneous TCSPC and static spectroscopy capabilities.

only consist of a pinhole to filter light but also a method of translating the collection and excitation optics with respect to the sample. By scanning these optics and collecting intensity information from individual points on the sample, it is possible to reconstruct an image of the sample. Furthermore, because the collected photons are restricted to a specific focal plane, it is possible to also change the focusing distance of the collection lens to get information along all three axes: x, y and z. Thus, confocal microscopes cannot only form two dimensional images but also three dimensional tomographs [65].

The requirement that single pixels are collected at any given time when using a confocal microscope makes these kinds of microscopes ideal for use in spectroscopy because spectroscopy is a single-point detection technique. By combining the scanning capability of the confocal microscope and the spectral analysis of a spectrometer, it is possible to make spatially resolved images of spectroscopic information with very high spatial selectivity. Furthermore, using beam splitters, it is possible to collect multiple types of data simultaneously with a confocal microscope. The standard microscope built for our studies combines both static spectroscopy with TCSPC, allowing both transient and static measurements to occur simultaneously. This setup is depicted in figure 4.3. Here the presence of fiber optics is particularly important because their core-cladding interface acts as the pinhole.

The capabilities of this basic microscope can be extended by including polarizing elements for polarization resolved measurements, as well as the inclusion of electromagnets and cryostats to house the sample for magnetic field and temperature resolved measurements. Multiple light sources can also be included, as well as imaging optics to collect wide field images. Hence, this basic microscope is easily modified and very versatile.

Chapter 5

Quantum Dot-Plasmon Interaction on Wrinkled Metal Surfaces

Förster Resonant Energy Transfer is useful as a spectroscopic ruler, as well as a promising mechanism for energy transfer in solar energy harvesting [29]. The main limitation of FRET is that, although the energy transfer can be very efficient, it is limited to single nanometer distances. In this chapter, we will discuss research on enhancing the energy transfer distance of FRET via coupling to localized surface plasmons. We will discuss the development of a substrate that supports plasmon excitations and the order of magnitude enhancement of energy transfer distance that results when quantum dots are deposited on it [19]. Furthermore, we will show how to identify plasmonic excitations on a surface using quantum dots and how to characterize plasmon travel distances using plasmon assisted FRET between quantum dots.

5.1 Plasmons & Localized Surface Plasmons

The free electrons in a metal subject to the electro-magnetic field of incident photons can behave collectively forming a charge density wave [5], called a plasma oscillation. When the thickness of a metal is thin enough such that it can be treated as a pseudo two-dimensional material, these plasma oscillations behave as a pseudo-particle called a plasmon. Assuming the metal is oriented in the x-y plane, a photon traveling toward the metal with some electric field component in the x-y plane will excite a plasmon subject to momentum and energy conservation [44]. The excited plasmon will travel in the same direction as the in-plane component of the photon's Poynting vector. The electric field generated by the plasmon will have a component along the direction it travels, as well as an out-of-plane component. Assuming the photon was traveling with some component in the x-direction, the electric field of the plasmon will be [58, 101]

$$E_x = \frac{A_x k_2}{\omega \varepsilon_0 \varepsilon_2} \exp(i(\beta x + \pi/2) - k_2 z - i\omega t) \tag{5.1}$$

$$E_z = \frac{-A_z \beta}{\omega \varepsilon_0 \varepsilon_2} \exp(i\beta x - k_2 z - i\omega t), \tag{5.2}$$

where A_i are the amplitudes in the i-th direction, β and k_2 are related to material constants and have both real and imaginary components, and ω is the frequency of the incident photon. Because β and k_2 are complex, the electric field will oscillate in both the x- and z- directions. Furthermore, the magnitude of the electric field will decay exponential away from the surface as well as along the direction of travel. Due to this exponential dependence, the plasmon field is called an evanescent wave. These waves are capable of traveling up to hundreds of microns with the correct combination of dielectrics and metals, but because of the exponential vertical distance dependence, anything coupling to the plasmonic excitations must be within a few tens of nanometers of the metal surface.

In the case when confinement occurs in three dimensions, plasma excitations will be highly localized, which is the case for metallic nanoparticles. Similar to quantum confinement in quantum dots, localized surface plasmons are excited at specific energies resulting in a narrow absorption spectrum [58].

5.2 Quantum Dot-Plasmon Interactions

In an analysis similar to that for FRET, we can describe the energy of the electric dipole of the QDs in the electric field of the plasmons as

$$\mathcal{H} = -\mathbf{E}_{\text{Plasmon}} \cdot \mathbf{D}_{\text{QD}}. \tag{5.3}$$

This plasmon field is oscillatory, so this Hamiltonian has a similar form to the interaction Hamiltonian of a photon with a dipole. Thus, plasmons can excite and be excited by electric dipole transitions. A key difference is that the amplitude of the electric field of the plasmon decays exponentially away from the metal surface. Therefore, QDs need to be close to the metal surface to couple to excited plasmons, usually within a few tens of nanometers.

From this analysis, we have a theoretical basis for the coupling of non-radiative interactions between two QDs in close proximity to a metal film. Conceptually, this interaction can be thought of this way:

1. A QD is put into an excited state.
2. The energy of the excited state is transfered to a surface plasmon.
3. The surface plasmon travels some distance eventually encountering a QD, thus exciting it.

Superficially, this process appears similar to a photon emission/reabsorption-type process and has a similar condition on energy in that the plasmon excitation from the donor must have a frequency that overlaps with the absorption spectrum of the acceptor. In fact, this process is more like FRET, which has the same spectral overlap requirement but is also distance dependent, and the excitation of the plasmon must occur on a timescale much faster than the radiative decay channel in order for it to occur. Because plasmons can propagate over micron scale distances, this kind of energy transfer can occur over much larger distances than FRET. Thus, we call this process plasmon mediated FRET or plasmon enhanced FRET.

5.3 Gold-Palladium Plasmon Cavities

A low-cost, high-throughput method of generating patterned metal surfaces was developed by the Khine Group [21]. These surfaces are generated by sputter coating a thin (30 nm thick) gold-palladium (AuPd) surface onto a thermoplastic, polydimethylsiloxane (PDMS). When the PDMS/AuPd substrate is heated, the PDMS contracts while the AuPd expands. The metal is restricted to the boundaries of the PDMS, so the metal buckles in order to satisfy boundary conditions. If only one parallel set of boundaries is allowed to contract, the metal buckles along only one direction, resulting in a corrugated surface (uniaxial buckling). If all four boundaries are allowed to contract, the metal buckles along both directions, resulting in flower-like meso-structures (biaxial buckling, inset figure 5.1a).

We are interested in identifying whether these structures result in localized surface plasmon resonance and if they can be used to enhance the electro-optical properties of fluorescent species. Confirming the existence of these behaviors would allow these substrates to be used in electro-optic applications like solar energy collection and plasmon-enhanced sensing. Due to the relatively inexpensive cost of PDMS, metal sputter targets, sputter coaters and ovens required to generate these substrates, these would be inexpensive alternatives to patterned metal substrates for plasmon-enhanced optical applications. Furthermore, the fabrication process takes minutes to complete, making them much faster and easier to fabricate than patterned surfaces. The downside of these substrates is that their structures are not uniform in size and shape, which can be detrimental to fundamental physics applications which usually require the well defined structures generated by micro-patterning.

5.4 Experimental Procedure

We generate biaxially structured AuPd surfaces and flat AuPd surfaces in addition to purchasing glass slides. We then spin coat a solution of cadmium selenide quantum dots capped with a zinc sulfide shell (CdSe/ZnS) on these surfaces. We use a range of concentrations-0.5 µmol, 0.1 µmol and 0.05 µmol-and a series of QDs with different radii between 1.9 nm-5.6 nm, i.e., five different ensembles of QDs with emission in the wavelength range 488 nm-620 nm.

We measure these samples in a custom-built confocal microscope capable of spatially resolved static and time-resolved spectroscopy of the QD emission. The microscope has a diffraction-limited spatial resolution of ~ 500 nm. For static spectroscopy, we excite the samples with a continuous wave diode laser emitting at 405 nm (Coherent Cube), and we collect emission spectra using an Acton 2-300i monochromator coupled to a PIXIS 400 thermoelectrically cooled charge-coupled device (CCD), which provides a spectral resolution of 0.02 nm. For time-resolved spectroscopy, we excite the sample with a frequency-doubled Ti:Sapphire laser (Coherent Mira 900-D) with emission tuned to 405 nm at 76 MHz with 150 ps pulses. We collect time resolved traces using a PicoHarp time-correlated single-photon counting module which has a temporal resolution of 4 ps. We collect absorption spectra with a Perkin Elmer UV-VIS spectrophotometer with 0.5 nm spectral resolution.

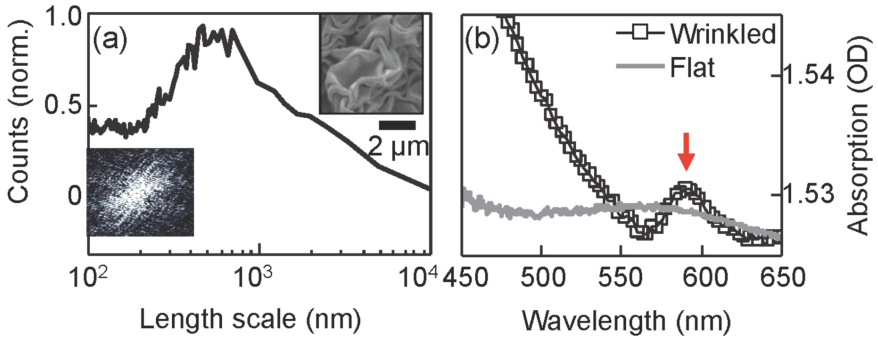

Figure 5.1: (a)(top inset) SEM image of a biaxial AuPd substrate, (bottom inset) 2D FFT of the SEM image, (center) probability distribution of the length scales present in the SEM. (b) Absorption spectra of flat and wrinkled AuPd substrates with an arrow indicating the LSP absorption peak of the wrinkled substrate. [19]

5.5 Results

5.5.1 Identifying the Signatures of FRET

To characterize the geometry of the substrates, we perform scanning electron microscopy (inset figure 5.1a). The length scales of the substrates are revealed by performing a 2D fast-fourier transform (FFT) and then radially integrating the transformed image to quantify the sample averaged length scales. The probability distribution of length scales present on the sample (figure 5.1a) demonstrates a diffuse background, indicating a continuum of length scales, with a broad peak centered around 500 nm extending between 200 nm and 1 µm. The biaxial structures are on the size scale of plasmon propagation. Optical absorption (figure 5.1b) of these structures shows a highly localized peak centered at 580 nm, which is expected for localized surface plasmon (LSP) excitations [98]. Optical absorption of flat AuPd substrates shows a response typical of surface plasmon excitations, which have a broad continuum of states [95].

We next deposit CdSe/ZnS QDs on the wrinkled substrates and perform scanning confocal spectroscopy. The data are first analyzed by plotting the wavelength at which each spectrum is maximum at every position, thereby generating a spatially resolved image of the redshift present on the sample, called a photoluminescence (PL) map, inset figure 5.2a. The preliminary data with a QD ensemble emitting at 544 nm show regions of redshift and no shift relative to the solution emission. Comparing spectra from these regions, we see that the low energy QDs in the redshifted region have enhanced emission intensity commensurate with energy transfer from high to low energy QDs (figure 5.2a) [56, 84]. We repeat these measurements with QDs of different sizes, allowing us to scan the QD emission spectrum through the substrate's absorption peak. In figure 5.2b, the maximum redshift seen in each PL map is plotted as a function of QD diameter. These data indicate the redshift is maximized for QD ensembles whose peak emission (586 nm) overlaps the substrate's absorption peak (580 nm), which corresponds with our understanding of the QD-plasmon coupling process which predicts energy transfer is maximized when the transition frequency of the QD is equal to the frequency of the surface plasmons.

This FRET-like behavior could be plasmon mediated, or it could be due to close packing of the QDs [55] by the structures on the substrate (unmediated FRET). The latter option is unlikely because the substrate is structured on the order of 10^2-10^3nm, while the QDs have diameters on

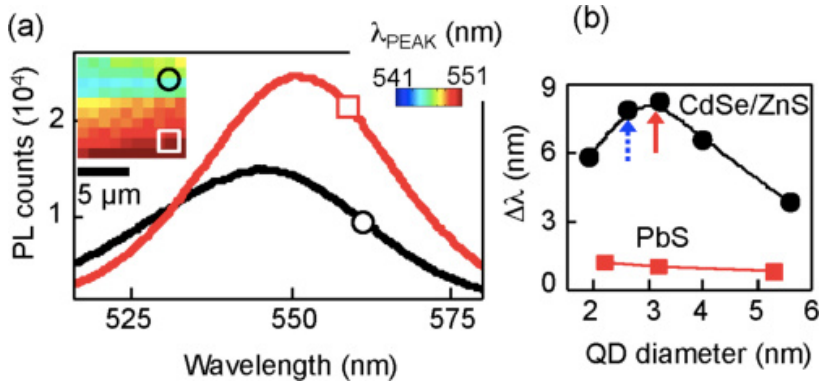

Figure 5.2: (a)(inset) PL map of peak emission wavelength (λ_{peak}) for QDs which emit at 544 nm in solution (center) Emission spectra from the two positions indicated by the square and circle symbols. (b) Maximum observed redshift ($\Delta\lambda$) as a function of QD diameter for CdSe and PbS QD ensembles. Arrows indicate QDs with (dashed arrow) 544 nm emission and (solid arrow) 586 nm emission in solution. [19]

the order of a single nanometer. We verify this assumption by depositing lead sulfide (PbS) QDs on these substrates. The PbS QDs have emission in the NIR but are on the same size scale as the CdSe/ZnS QDs. Furthermore, when close packed, a 40 nm redshift has been observed for PbS QDs as a result of FRET [14], so if there is close packing the redshift observed should be more dramatic with the PbS. When we generate PL maps and extract redshift data for these samples, we find that there is almost no redshift, indicating the absence of FRET between these dots (figure 5.2b). Consequently, they are not close packing and because their emission does not overlap the substrate absorption, there is also no plasmon-mediated FRET between them. This test eliminates the possibility that close packing by the substrate is causing FRET between the CdSe QDs, and FRET is likely the result of plasmon mediation.

5.5.2 Verifying and Analyzing the Plasmon-Mediated FRET

We can quantify the strength of the FRET process by comparing the emission of the donor and acceptor populations within the ensemble. We do this by fitting the emission spectra of the QDs with a bimodal Gaussian distribution, in the approximation that the Lorentzian character of the dipole transitions is negligibly wide relative to the width of the inhomogeneously broadened ensemble spectrum. Comparing the areas of the donor and acceptor emissions will provide a figure of merit for the strength of the FRET process. We perform this test by depositing CdSe/ZnS QDs which emit at 586 nm on a glass slide, a flat AuPd substrate and a biaxial AuPd substrate. We generate PL maps for each of these substrates (figure 5.3a-c), which indicate the emission of these QDs peaks at 586 nm on the glass slide. On the flat metal, there is a uniform redshift from solution emission, but the redshift is on the order of 1 nm. Finally, on the wrinkled metal, we observe uniform redshifting on the order of 10 nm. Therefore, we hypothesize that the donor emission is most strongly suppressed on the wrinkled metal due to FRET. In figures 5.3d-f, we have extracted representative emission spectra from each of these samples. Fitting the bimodal Gaussian model to them, we find that the donor emission is almost completely suppressed on the wrinkled metal. Furthermore, on the wrinkled metal, the acceptor emission is enhanced by nearly a factor of three relative to the glass slide, commensurate with FRET. There is nearly a factor of two enhancement on the flat metal,

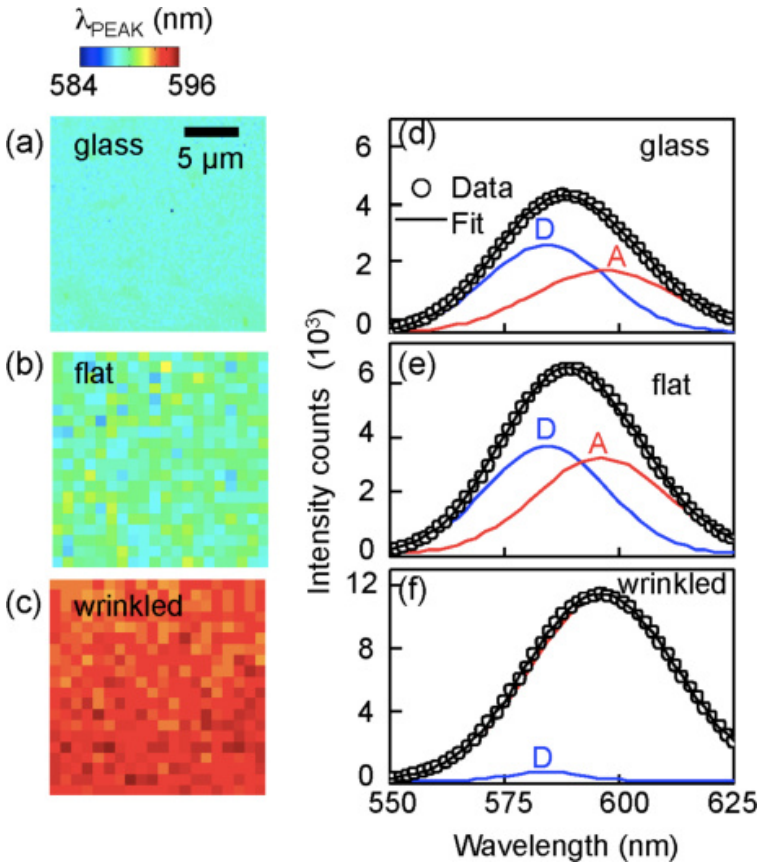

Figure 5.3: PL maps of QDs with solution emission of 586 nm deposited on (a) glass, (b) flat AuPd and (c) wrinkled AuPd. Bimodal Gaussian fits deconvoluting emission from donor (blue) and acceptor (red) QD populations on (d) glass, (e) flat AuPd and (f) wrinkled AuPd. [19]

indicating that coupling to LSPs provides a greater enhancement than the surface plasmons present on the flat metal.

As previously discussed, in addition to the static spectral changes, we expect to see a secondary decay channel in time-resolved spectroscopic data in the presence of FRET [87] due to the requirement that any energy transfer processes must be faster than the radiative decay channel in order for them to be probable decay modes. We perform TCSPC on each of the previously discussed samples and plot their intensity-normalized time-resolved traces (figure 5.4). The data taken on the glass slide is well modeled by a single exponential decay with $\tau = (11.0 \pm 0.3)$ ns, further indicating a lack of close packing at the QD solution concentration. The data taken for the QDs on the metal substrates are properly modeled by a bi-exponential decay as expected for QD-plasmon coupling. The mean radiative decay and plasmon-coupling lifetimes are given in table 5.1. The non-radiative decay rate increases on the wrinkled metal, confirming that energy transfer becomes more probable on this substrate and corroborating the results of the analysis of the static fluorescence spectroscopy. Thus, there is energy transfer on the wrinkled metal substrates and it is plasmon mediated.

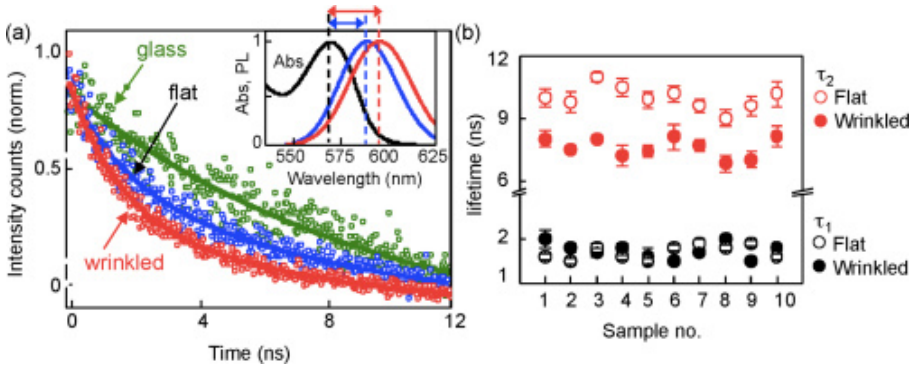

Figure 5.4: (a)(inset)Normalized QD emission on (blue) glass and (red) wrinkled surfaces overlayed (black) with normalized QD absorption on glass depicting emission/absorption overlap due to stokes shifting. (center) TCSPC traces of QDs on (green) glass, (blue) flat and (red) wrinkled surfaces. (b) Radiative (τ_2) and non-radiative (τ_1) lifetimes measured on 10 different flat (open circles) and wrinkled (closed circles) samples. [19]

Table 5.1: A comparison of radiative and plasmon-coupling lifetimes for CdSe/ZnS QD ensembles emitting at 586 nm on glass and flat and wrinkled metals.

Substrate	$\tau_{\text{radiative}}$(ns)	τ_{plasmon}(ns)
Glass	11 ± 0.3	–
Flat AuPd	10 ± 0.4	2 ± 0.2
Wrinkled AuPd	8 ± 0.4	1.6 ± 0.07

Table 5.2: A QD concentration dependence correlating inter-dot spacing to spectroscopic redshift.

Concentration (µmol)	Mean Particle Distance (nm)	Observed Spectral Redshift (nm)
0.05	30-40	0
0.1	20-25	3-5
0.5	10-15	8-10

5.5.3 Distance Dependence of Plasmon-Assisted FRET

Our final set of measurements concerns quantifying how much plasmon resonance enhances the distance dependence of FRET. In an attempt to quantify the mean interparticle distance, we SEM and AFM our samples. Unfortunately, SEM resolution is not high enough to detect the QDs, and the AFM tips are not able to fit into and follow the wrinkles in the metal. Thus, we use an indirect method to quantify interparticle distances. Under the assumption that the mean interparticle distance is approximately the same for solutions deposited on glass and wrinkled substrates, we perform a concentration-dependent study of this phenomenon on glass and wrinkled metals. We generate three QD solutions of ensembles with a peak emission wavelength of 586 nm: 0.05 µmol, 0.1 µmol and 0.5 µmol. After depositing these samples on glass, we TEM the ensemble to determine the mean interparticle distance. We then construct PL maps for the solutions deposited on the wrinkled metal and glass (figure 5.5) to determine the amount of redshift for each solution. The results are summarized in table 5.2. For the highest concentration, 0.5 µmol, the interparticle spacing is in the 10 to 15 nm range, which correlates to almost complete quenching of the donor emission and complete enhancement of the acceptor emission, which is indicated by an 8 to 10 nm

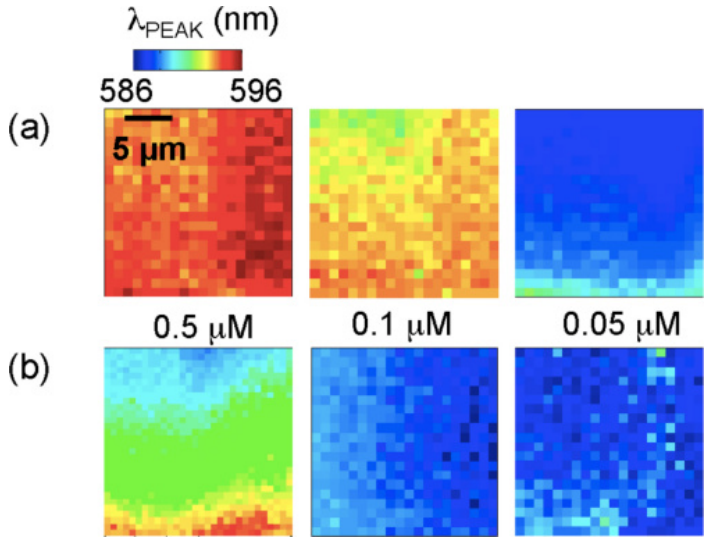

Figure 5.5: PL maps of QDs with solution emission of 586 nm deposited on (a) wrinkled metal and (b) glass at three different solution concentrations. [19]

redshift of the ensemble emission. This result further substantiates the claim that localized surface plasmons are mediating the energy transfer between donor and acceptors because unmediated FRET between these particles has an upper distance limit of 10 nm between donors and acceptors [13]. Furthermore, as we decrease the solution concentration, the interparticle spacing increases to a maximum of 30 to 40 nm, at which point we observe no energy transfer. Thus, plasmon-mediated FRET is also distance dependent, but the distance scale of the phenomenon is increased by an order of magnitude over unassisted FRET. This distance dependence is likely limited by the substrate because the propagation length of plasmons is a function of the plasma frequency of the metal and the dielectric constant of the PDMS. Therefore, because energy transfer distance is limited to 40 nm on this substrate, we can infer that the plasmon travel distance is also on this scale.

5.6 Conclusion & Future Directions

In an effort to increase energy transfer efficiencies in photonic devices, we fabricated and characterized microstructured AuPd surfaces. These structures support localized surface plasmon resonances. By depositing semiconductor nanoparticles on these surfaces, we were able to verify the existence of localized surface plasmon resonances. We found that these quantum dots transfer energy to plasmon excitations, and the plasmons are then capable of transferring energy to the quantum dots. This plasmon mediated FRET mechanism is optimized by spectral overlap between donor emission and plasmon/acceptor nanoparticle absorption. This process is also distance dependent with a maximum distance around 30 to 40 nm which is an order of magnitude increase over normal FRET. Furthermore, this indicates that plasmon excitations have a maximum travel distance around 40 nm on a 30 nm thick, AuPd wrinkled metal surface deposited on PDMS.

In the future, this work can be extended by generating different metal alloys and using different thermoplastics to maximize plasmon travel distances. Furthermore, the wrinkle dimensions can be

controlled by baking these samples for different amounts of time, which would allow future researchers to tune the location of the plasmon resonance absorption peak. Thus, studies can also be performed to generate a range of substrates to optimize energy transfer between emitters of different energies. One import regime for such a study is designing a substrate with plasmon resonance in the infrared, which would be valuable for Surface Enhanced Raman Spectroscopy (SERS) studies.

One other direction to take this research would be to generate substrates which are allowed to shrink only along one direction, which generates uniaxial wrinkles. Similar studies described in the previous paragraph could be performed. Due to the anisotropy of the wrinkles, it is conceivable that energy transfer between emitters would be preferentially along the wrinkle direction, i.e., the substrate acts as a plasmon waveguide. This kind of study could provide a route for increasing the efficiency of die sensitized solar cells.

In conclusion, we find that there is FRET-like electronic coupling between nanoparticles on these surfaces, and that this process is mediated by local excitations of the surface's free electron gas. Finally, because the propagation lengths of plasmons are material dependent, there is a mechanism for tuning the behavior of this process by changing the combination of metals, thermoplastics and QDs used to suit the required application, e.g., solar energy collection.

Chapter 6

Optical Effects of Spin Liquid Phases on Neodymium (III) in GGG

Strongly correlated electronic systems have become a particularly important field for the development of fundamental physics and next generation technologies. Of interest are strongly correlated magnetic systems that can develop exotic magnetic phases, which have applications in refrigeration and quantum computing. In this chapter, we will discuss optical measurements on a crystal, gadolinium gallium garnet (GGG), which has geometrically frustrated magnetic phases. Specifically, it has a spin liquid phase and a spin protectorate phase. We will show that information about the spin liquid phase can be collected optically via the interaction of the spin liquid phase and dopant ions (neodymium (III)), which act as a local probe for magnetic measurements within the GGG lattice.

6.1 Geometrically Frustrated Magnetism

Geometrically frustrated magnetic phases develop from a combination of rules for magnetic moment orientation and a lattice that does not allow these rules to be satisfied. The simplest example of this is the spin liquid phase, which can be seen on a lattice of triangles with anti-ferromagnetic Ising spins. In this model, we have spins that can point either up (+1) or down (-1) situated on the corners of an equilateral triangle. The energy of this configuration is

$$\mathcal{H}_{\text{Ising}} = -J \sum_{nn} S_i S_j, \tag{6.1}$$

where J is called the exchange energy, S_n is the spin (± 1) of the n-th spin, and nn indicates the sum is over nearest neighbors. If J is negative, the lowest energy for this system is attained when all nearest neighbors are anti-parallel, i.e., anti-ferromagnetic (AFM) coupling. On an equilateral triangle, it is not possible for every spin to satisfy the AFM coupling requirement simultaneously, thus the lowest energy state is degenerate (figure 6.1). Because this degeneracy is a result of the geometry of the lattice, this phenomenon is called geometrically frustrated magnetism.

When a crystal is in this phase, the degeneracy prevents the crystal from settling into a specific ground state at 0 K, so the crystal fluctuates through microstates of the ground state manifold [1].

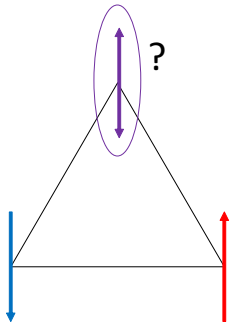

Figure 6.1: Ising spins on an equilateral triangle with anti-ferromagnetic coupling. Both the up and down states of the purple spin are degenerate.

The degeneracy also scales with the size of the system, so on an infinitely large lattice, there are an infinity of microstates in the ground state manifold. Furthermore, this phase is also characterized by a lack of long-range order [66], unlike a true anti-ferromagnetic order, which has spin correlations on the order of the size of the system at 0 K. Thus, traditional magnetic imaging techniques like magnetic circular dichroism sensitive images cannot detect the magnetic behavior of the system because any order in the system is far below the diffraction limit.

The qualitative behavior of the 2D anti-ferromagnetic Ising model is also seen in more general models that are more applicable to real systems. To understand GGG, we have to use the Heisenberg Hamiltonian:

$$\mathcal{H}_{\text{Heisenberg}} = -\sum_{nn} J(\mathbf{r}_{ij})\mathbf{S}_i \cdot \mathbf{S}_j, \tag{6.2}$$

where $J(\mathbf{r}_{ij})$ is called the exchange integral, which quantifies the spatial overlap of the wavefunctions of neighboring spins, and $\mathbf{S}_n$ is the vector operator that represents some angular momentum quantity of n-th ion. For rare earth ions in a crystal, these vector operators are the total angular momentum operator $\mathbf{J}$. To alleviate the inevitable ambiguity that will arise from calling the exchange integral J, we will relabel it ξ_{ij}.

In this model, a negative value of ξ_{ij} will again result in anti-ferromagnetic coupling. Because these spins are treated as 3D vectors, more complex behaviors can arise. We will now expand the Heisenberg Hamiltonian to illustrate this added complexity:

$$\mathcal{H}_{\text{Heisenberg}} = -\sum_{nn} \xi_{ij}(J_x^{(i)}J_x^{(j)} + J_y^{(i)}J_y^{(j)} + J_z^{(i)}J_z^{(j)}). \tag{6.3}$$

From this expanded Hamiltonian, we can see that if we neglect the x- and y-components of the total angular momentum, this Hamiltonian reduces to the Ising model where the z-direction is the quantization axis. Interactions are therefore, between M_J microstates of the Russel-Saunders term symbols of the nearest neighbor ions. If the microstates of the ion are degenerate, we recover the spin liquid phase seen in the Ising model and its dynamics. With the introduction of x- and y-components of the total angular momentum, the magnetic moments of the interacting ions can cant into the x-y plane. Depending on the lattice, this can result in a well ordered magnetic ground state that is not frustrated. On a properly structured lattice, these extra terms can result in procession of the magnetic moments about the z-axis [75, 105]. This is known as a weathervane mode. Thus, not only does spontaneous spin flipping occur down to 0 K, but also spin procession.

Practically, frustrated magnetic phases do not exist at all temperatures within a material. Thermal energy in the lattice acts to randomize magnetic moments. When the temperature of the lattice surpasses the energy scale of the exchange integral, the crystal typically enters a paramagnetic phase. The temperature at which this phase transition occurs is called the Curie-Weiss temperature (Θ_{cw}) [69]. There is also typically a low temperature limit as well, below which crystals tend to enter disordered phases or cooperative phases with some order. The ratio of the Θ_{cw} to the low temperature phase transition temperature is called the frustration index:

$$f = \frac{|\Theta_{cw}|}{T}, \tag{6.4}$$

where Θ_{cw} is in absolute values because it is negative for anti-ferromagnetic crystals. The frustration index is simply a figure of merit to quantify how "frustrated" a lattice is. The larger the frustration index, the more frustrated a crystal is, with a limit at $+\infty$ which indicates the crystal remains a spin liquid to 0 K. Typically, values of five or greater indicate the presence of a frustrated magnetic phase [25].

6.2 Gadolinium Gallium Garnet

Gadolinium gallium garnet is a rare earth ionic crystal with garnet structure. It has fundamental importance to technological development because it is a durable ceramic with almost no absorption in the optical spectrum [100]. It is primarily used in two applications: as a host for laser gain media [57] and as a substrate for magnetic memories [31]. It has also been of fundamental importance to the study of frustrated magnetism because it was one of the first materials discovered with a spin liquid phase. Thus, our optical study of spin liquid materials uses this material because its spin liquid phase is well characterized and because other exotic types of magnetic phases exist in this material that we could potential investigate.

GGG crystalizes in space group $Ia\overline{3}d$, which is body center cubic with lattice constant $a = 12.382\,90\,\text{Å}$ [78]. The unit cell (figure 6.2a) contains 24 gadolinium ions, 40 gallium ions and 96 oxygen ions, for a total of 203 ions in the unit cell. Isolating the trivalent gadolinium sublattice, we see that the gadolinium ions form a network of corner-sharing equilateral triangles (figure 6.2b), which is topologically equivalent to a kagome tiling (figure 6.2c), typically called a hyper-kagome lattice [52]. Gd^{3+} has the electron configuration [Xe]$4f^7$ with ground state term Symbol $^8S_{7/2}$, and is therefore, a Kramer's ion. Because it is a Kramer's ion, the $\pm M_J$ degeneracy remains regardless of the crystal field symmetry, so "up" and "down" states are still accessible. The nearest neighbor exchange interaction $\xi_{ij} = -1.5\,\text{K}$ [80], indicating the Gd ions couple anti-ferromagnetically. Therefore, this crystal satisfies the anti-ferromagnetic interaction and lattice geometry requirements for a spin liquid phase, which it has below $\sim 2\,\text{K}$ [70, 71].

This crystal has several other magnetic phases. With no externally applied magnetic field, below 150 mK this crystal enters what has been termed a spin protectorate phase [23]. In this phase, islands of aligned magnetic moments develop in the spin liquid phase. These islands are non interacting and behave similarly to macroscopic spin systems like magnetic iron-oxide nanoparticles. They are theorized to nucleate on defect regions in the crystal. With an applied magnetic field below 2 K, the crystal enters a long-range ordered anti-ferromagnetic phase [32].

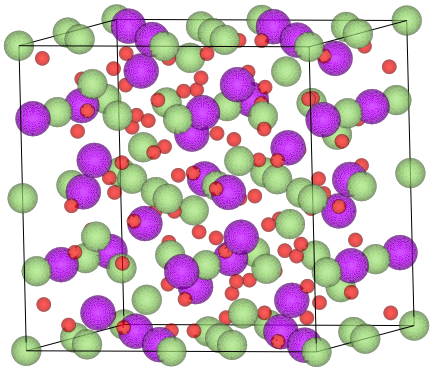

(a)

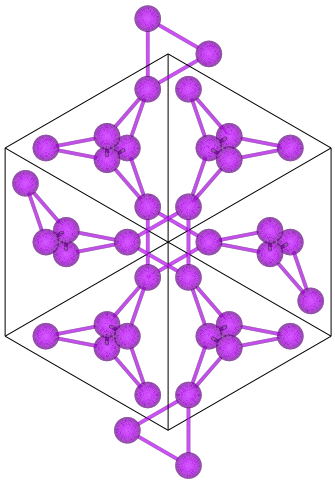

(b)

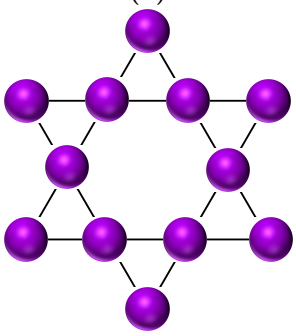

(c)

Figure 6.2: (a) A unit cell of GGG. The spheres indicate: (purple) gadolinium, (green) gallium and (red) oxygen ions [63]. (b) The Gd sublattice of GGG projected along the [111] direction. (c) An example of the 2D kagome tiling.

6.3 Neodymium-doped GGG

In order to explore the spin protectorate phase of GGG, we need a method that is capable of exploring the local environment of a protectorate at the time scales at which spin dynamics are likely to occur. Currently, AC magnetic susceptibility measurements are capable of measuring near the time scales necessary, but it measures the average response of the crystal, which includes the background spin liquid dynamics. Other techniques, like neutron scattering and muon scattering, are capable of probing locally but not at the nano- to picosecond time scales at which dynamics are hypothesized to occur. Thus, we need to develop a technique to probe the local environment of a crystal in the ultra-fast regime.

Ultra-fast optical measurements are a mature and well developed technique for these time scales. Unfortunately, due to the diffraction limit, optical measurements are limited to measuring on the length scale of hundreds of nanometers. To overcome this limit, we use an optically active, magnetic dopant as a local probe. The behavior of this probe can be measured using ultra-fast measurements, and at low concentrations single dopants can be measured to provide truly local information.

We use trivalent neodymium as our probe. Nd^{3+} has several properties that make it ideal for this system:

1. It is a Kramer's ion with ground state $^4I_{9/2}$, so if it couples to the spin liquid phase, it will be capable of cooperating in the spin dynamics.

2. Its ionic radius (112.3 pm) is similar to Gd^{3+} (107.8 pm) [82], so it minimally distorts the GGG lattice.

3. It emits in the NIR, so its transitions are easily accessible spectroscopically.

For this study, we purchase neodymium-doped GGG (Nd:GGG) in three different concentrations: 1.0, 0.5 and 0.1 at. %. At the highest dopant level, there is less than one dopant ion per unit cell[1] of the crystal. Thus, any Nd-Nd interactions are unlikely to occur in any of these samples. Neodymium ions preferentially substitute for gadolinium in this lattice. If they do not disrupt the spin liquid phase, they will be actively participating in the frustrated phase, which departs from a previous study on manganese-doped GGG. Because manganese is a transition metal, so it substitutes for gallium, which means it is not a member of the sublattice that forms the spin liquid phase. Linebroadening was observed for this sample at low temperatures, which was attributed to manganese coupling to the spin liquid phase [12]. Thus, dephasing should also be seen in the Nd spectrum and because it substitutes Gd, its dynamics will be correlated with the dynamics of the spin liquid phase.

6.3.1 Spin Liquid Behavior Enhancement

Measurements to confirm that the neodymium dopant does not disrupt the spin liquid phase were performed by collaborators at the University of Chicago. They measured the AC magnetic susceptibility of undoped and doped samples. AC magnetic susceptibility is capable of measuring the effects of driving fluctuating magnetic systems. This technique is similar to performing an optical absorption measurement in that an oscillating magnetic field is applied to a sample. The

[1] #Nd per unit cell = 1.0 at % × 24 Gd ions per unit cell = 0.24 Nd per unit cell

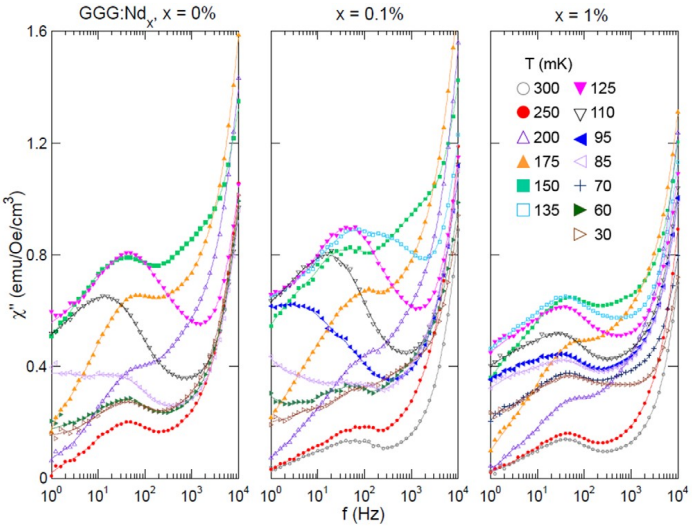

Figure 6.3: Imaginary component of AC Magnetic Susceptibility of undoped and Nd doped GGG plotted as a function of driving frequency and temperature, showing broad peaks around 50 Hz resulting from the spin liquid phase [99].

frequency of the AC magnetic field is swept, and the complex magnetic susceptibility of the sample is recorded. The imaginary component of the AC magnetic susceptibility is related to energy dissipation mechanisms [61], similar to how the optical absorption of a sample is the imaginary component of the dielectric tensor [6].

The signature of a spin liquid phase in AC magnetic susceptibility is a diffuse peak in the imaginary susceptibility owing to the range of time scales on which spin fluctuations can occur. The temperature and concentration-dependent imaginary component of the AC magnetic susceptibility of Nd:GGG is plotted in figure 6.3. At the highest temperature measured (300 mK), which is well within the spin liquid phase of GGG, the spin liquid response is observed in the doped samples. As the sample is cooled further, this response disappears for the undoped sample but persists to lower temperatures for the doped samples. Thus, the doped samples have a higher frustration index than the undoped samples, indicating that the Nd dopant enhances the frustration in the Gd sublattice rather than disrupting it [99].

6.3.2 Neodymium (III) Energy Level Structure

The Gd site Nd occupies as a dopant has point group symmetry D_2 (orthorhombic, figure 6.4a), which fully lifts the ten-fold degenerate $^4I_{9/2}$ ground state and four-fold degenerate $^4F_{3/2}$ first excited state up to Kramer's degeneracy. Thus, the optical spectrum of the first excited to ground state transitions will consist of ten lines.

Furthermore, with low probability, Nd will substitute for Ga in what will be considered an anti-site defect[2]. Gallium takes two inequivalent Wyckoff positions within the lattice, one with S_4 (tetragonal, figure 6.4b) point symmetry and the other with C_{3i} (trigonal, figure 6.4c) point symmetry. These point groups also have low enough symmetry to fully break the degeneracy of

[2] An anti-site defect is when an atom takes the place of a different atom within the lattice.

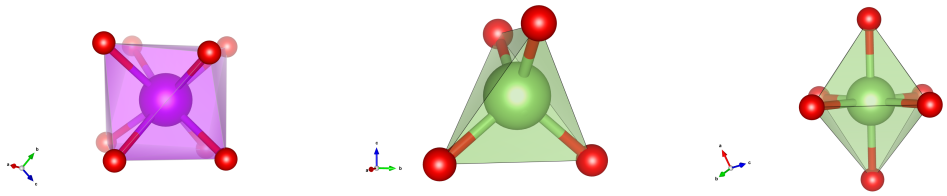

(a) (b) (c)

Figure 6.4: The oxygen ligand positions surrounding the sites of (a) D_2, (b) S_4 and (c) C_{3i} point symmetry.

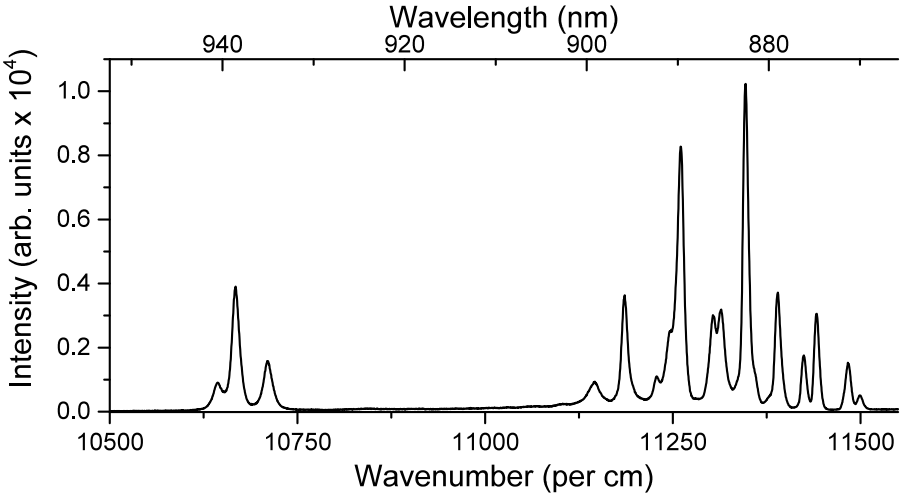

Figure 6.5: Emission spectrum of Nd^{3+} in GGG doped to 1 at. % concentration at $T = 50\,\mathrm{K}$.

trivalent neodymium's ground and first excited states. This is particularly true because Ga and Nd have vastly different ionic radii, thus the point symmetry of these positions is likely lowered even further due to lattice distortions. Therefore, there will be ten transitions present in the emission from each of these anti-site defects. Overall, the total emission summed over each of the three crystal positions results in 30 spectral lines.

Finally, as macroscopic crystals, there is expected to be a wide distribution of crystal defects that result in stress and strain in the crystal. Therefore, the optical spectrum measured from these samples will consist of 30 inhomogeneously broadened lines, resulting from crystal strain, and the ten transitions emitted from the three crystallographic positions the Nd ions occupy. A raw spectrum of these levels is plotted in figure 6.5. These 30 transitions are present but heavily overlapping, thus Voigt fits are necessary to deconvolute each of these transitions.

6.4 Experimental Procedure

To detect the optical signature of the influence of the spin liquid phase on neodymium, we cool the samples while monitoring the emission from the ${}^4F_{3/2} \rightarrow {}^4 I_{9/2}$ transition. AC magnetic susceptibility confirmed that these samples have a spin liquid phase, thus the ground state of Nd must be participating in it. Due to the spin fluctuations arising not only from the spin-flipping from the $J_z^i J_z^j$ coupling but also the fluctuations in the x- and y-components of these operators, we expect

the spin liquid phase will behave as a dephasing mechanism, which means it causes homogeneous broadening of the optical spectrum.

To perform this study, we place the Nd:GGG crystals in a cryostat capable of achieving temperatures of 5 K. The samples are excited using a Coherent Mira 900-D Ti:Sapphire laser tuned to 808 nm, which is resonant with the absorption peak of the ground-to-second excited state transition. In contrast to the experimental procedure of the previous chapter in which we used higher excitation energy than the energy gap between the ground and excited state, here we choose to use near-resonant excitation. Exciting an atomic system with energies larger than the ground state absorption peaks results in the atom entering a highly excited state. We choose this near-resonant excitation because decay pathways from these highly excited states usually generate phonons. Energy difference between highly excited states are small as a result of the inverse n^2 dependence of the eigenenergies of the hydrogenic Hamiltonian. These small energy differences typically have the same energy scale as the phonon density of states, which is why decay via phonon emission is likely to occur. These phonons modify the optical properties of ions in the crystal, as seen in figure 6.6a which exhibits a broad, diffuse background and quenched emission under high energy (532 nm) excitation as compared to near-resonant (808 nm) excitation. Furthermore, phonons generated as a result of high energy excitation can cause the GGG to remain paramagnetic, resulting in the disruption of the spin liquid phase. Therefore, we use near-resonant excitation because it minimally affects the optical properties of the probe ions and the magnetic state of the lattice.

Under near-resonant excitation the Nd ions are excited to the $^4F_{5/2}$ state which decays via the emission of an optical phonon, which has an energy of 882 per cm, to the $^4F_{3/2}$ first excited state (figure 6.6b). Under the low excitation power (20 µW) used in this experiment, the single phonon generated under this excitation scheme negligibly effects the Nd emission spectrum. We use an Acton 2-300i spectrometer coupled to a thermoelectrically cooled PIXIS 100 CCD, which measures the spectra with a resolution of 0.2 cm^{-1}. Because we are interested in quantifying the homogeneous broadening of these samples with the best possible accuracy we measure the fluorescence spectrum in units of wavenumbers to remove asymmetry caused by using wavelength.

The stark split levels of the $^4I_{9/2}$ manifold, labeled $Z_1 - Z_5$, and the levels of the $^4F_{3/2}$ manifold, labeled R_1 and R_2, are closely spaced. Thus, there is a high degree of spectral overlap between the Z_1 through Z_4 levels. The Z_5 level is separated substantially from the other levels in the ground state manifold. As a result, we choose to track the emission of the $R_n \rightarrow Z_5$ levels. This has a couple of benefits:

1. The energy separation between the Z_4 and Z_5 level is on the order of 750 K; consequently, thermal excitation between Z_1–Z_4 to the Z_5 level will not be an effect that needs to be accounted for at the temperature scales of the measurement.

2. Data analysis does not need to include the other transitions in the manifold (figure 6.6c), so fits to the data are more accurate than fits to the other transitions, which would require fitting 24 transitions simultaneously as opposed to six.

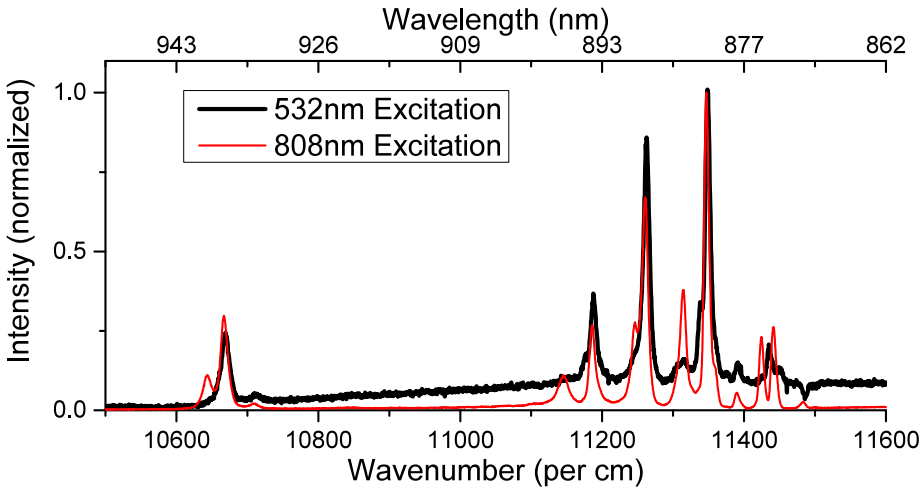

(a)

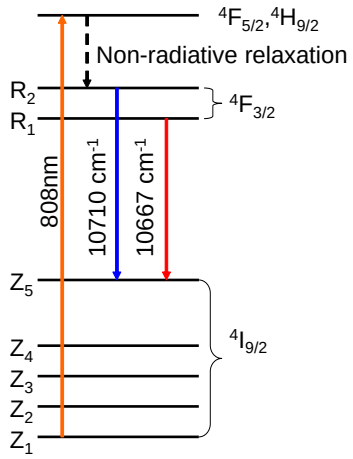

(b)

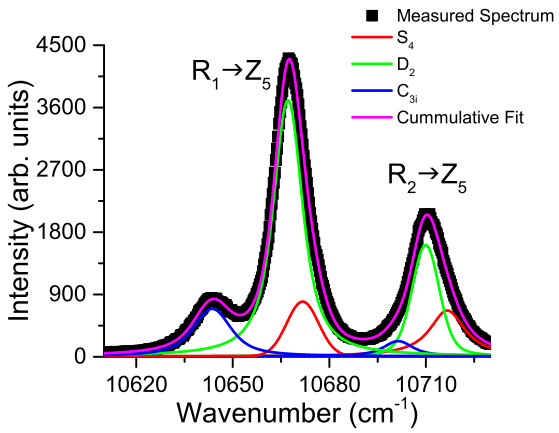

(c)

Figure 6.6: (a) A comparison of the Nd^{3+} emission under 532 nm and 808 nm excitation at 10 K with 1 at. % doping concentration. (b) Energy level diagram of Nd^{3+} in GGG indicating the excitation (orange arrow) and decay pathways (blue and red arrows) being measured. (c) The spectrum of the Z_5 transitions at 50 K with 1 at. % doping concentration. The solid lines are Voigt fits to the transitions from each of the inequivalent crystal positions that Nd can occupy.

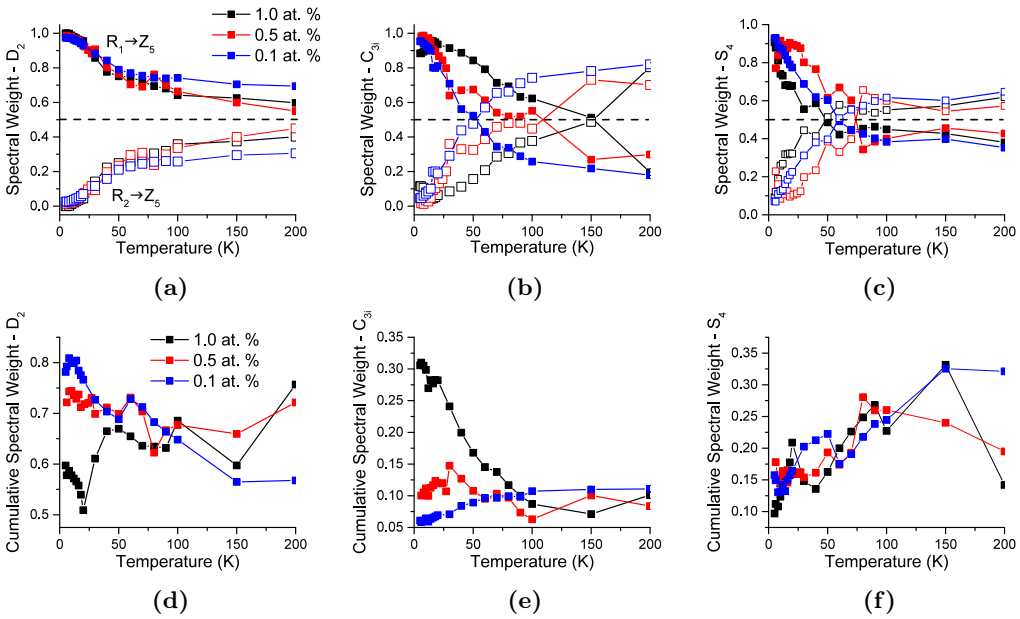

Figure 6.7: (a-c) The spectral weight of the R_1 (closed squares) and R_2 (open squares) to Z_5 transitions originating from the D_2, C_{3i} and S_4 crystallographic positions as a function of temperature and concentration. The dashed line indicates 50%. (d-f) The cumulative spectral weights of the total emission from each of the crystallographic positions in the set of Z_5 transitions as a function of temperature and concentration.

6.5 Transition Spectral Weight

To confirm our interpretation that the six peaks in the $R_n \rightarrow Z_5$ spectrum are from anti-site dislocations rather than some other defect, like the presence of another kind of atom, we track the spectral weight of each transition. The first set of spectral weight analysis is calculated by taking the area parameter of the Voigt fits and computing the total area of each set of R-lines for each lattice position the Nd ions can occupy. We then divide the area of each transition by the total area of the set it belongs to:

$$\mathrm{SW}(q,n) = \frac{A^q_{R_n}}{A^q_{R_1} + A^q_{R_2}}, \text{ where } q \in \{D_2, C_{3i}, S_4\}. \tag{6.5}$$

With this calculation we directly compare the area of each transition at every lattice position, temperature and concentration. Plotting these spectral weights (figure 6.7), we find that the spectral weight of the $R_1 \rightarrow Z_5$ and $R_2 \rightarrow Z_5$ lines generally follow the same trends, with slight deviations occurring between the different lattice positions. Specifically, these spectral weights follow the trend observed for thermal depopulation of a two-level system, i.e., Fermi-Dirac statistics. In this case, the two-level system is the R_1 and R_2 levels of the excited state. Furthermore, because we see this same functional form, rather than another functional form, not only in the transition for Nd occupying the D_2 position but also for the C_{3i} and S_4 positions, we deduce that these transitions result from Nd occupying other lattice positions.

Next, we can compare the total area of the transitions at each lattice position to the total area of the six observed lines. This comparison gives us a way to compare the intensity of anti-site emission to the emission intensity from the proper dopant position. We will call this quantity the cumulative

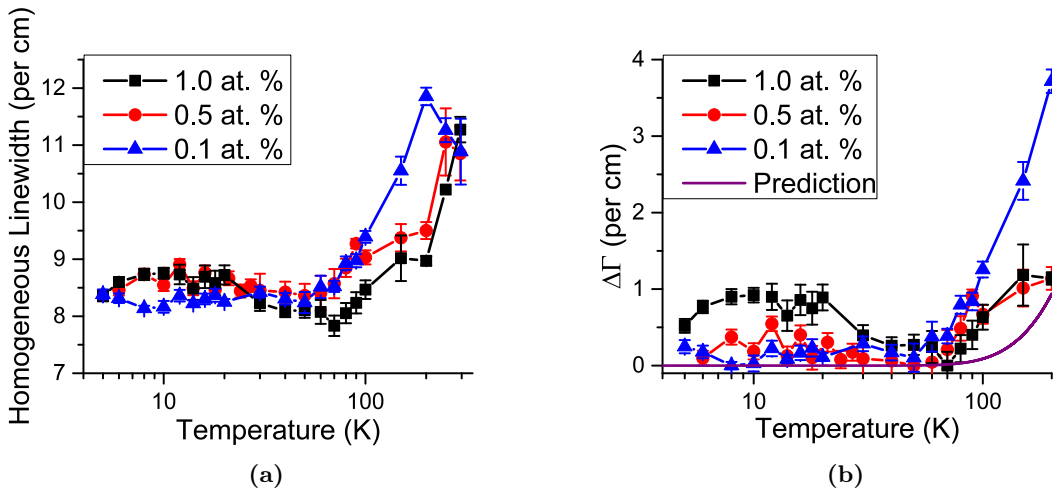

Figure 6.8: (a) The homogeneous linewidth of the $R_1 \rightarrow Z_5$ transition as a function of temperature for three doping concentrations. (b) A comparison of the anomalous linebroadening at low temperatures to the broadening predicted for the Raman scattering mechanism.

spectral weight:

$$\mathrm{CSW}(q) = \frac{A^q_{R_1} + A^q_{R_2}}{A^{D_2}_{R_1} + A^{D_2}_{R_2} + A^{C_{3i}}_{R_1} + A^{C_{3i}}_{R_2} + A^{S_4}_{R_1} + A^{S_4}_{R_2}}, \text{ where } q \in \{D_2, C_{3i}, S_4\}. \tag{6.6}$$

The most noticeable trend is the decrease in the cumulative spectral weight of the emission from the D_2 site with increasing dopant concentration. This behavior corresponds to a relative spectral weight increase of the C_{3i} site with dopant concentration. In fact, the increase in cumulative spectral weight at low temperature for the C_{3i} site corresponds to a linear trend with a slope of 0.005 in units of spectral weight per concentration. This correspondence suggests that at higher dopant concentrations, this defect site has a higher probability of being occupied. Interestingly, the cumulative spectral weight of the S_4 site stays constant with increasing dopant concentration. This is likely because there are 24 C_{3i} positions and 16 S_4 positions within the unit cell making the C_{3i} site more likely to be occupied than the S_4 site.

6.6 Optical Signature of Nd-Spin Liquid Coupling

As we cool the samples, the homogeneous linewidth of the $R_1 \rightarrow Z_5$ transition narrows as expected when phonons freeze out of the crystal. Below 30 K the homogeneous linewidth begins to broaden and continues to do so down to the lowest measured temperatures (figure 6.8a). This broadening is contrary to the behavior observed in other neodymium (III)-doped crystals in which the homogeneous linewidth of this transition narrows to a constant value at the lowest temperatures, a result accounted for by the Raman scattering mechanism [50, 96].

In figure 6.8b, we subtract the narrowest linewidth achieved to highlight the broadening behavior below 100 K. Super-imposed we have plotted the linebroadening caused by the Raman scattering process, assuming the debye temperature of the crystal is that of GGG ($T_D = 520$ K) with a typical value for the coupling constant for rare-earth doped garnets ($W = 0.1$). Notice that the Raman

scattering process completely freezes out by 80 K and has no low temperature broadening in the region where anomalous broadening is observed. Thus, the broadening is not caused by the process which normally causes dephasing in other Nd-doped crystals. Furthermore, the effect is most dramatic for the 1.0 at. % doped sample, which is commensurate with the AC magnetic susceptibility data which indicates this sample has the largest frustration index.

6.6.1 Nd:GGG Temperature Dynamics

From the homogeneous broadening data, we see that anomalous broadening begins around 40 K, which is much higher than the paramagnetic-to-spin liquid transition temperature of GGG (2 K). This discrepancy can be caused by islands of spin liquid phase nucleating in the paramagnetic phase. As the temperature of the crystals is reduced, these islands begin to grow until the spin liquid phase transition where most of the lattice is in the spin liquid phase and where we expect the homogeneous linewidth to plateau at some value higher than the natural linewidth of the transition. This interpretation is supported by Monte Carlo simulations of classical Heisenberg anti-ferromagnets on a hyper-kagome lattice [105] and a Spin-1/2 Kitaev anti-ferromagnet on a honeycomb lattice [66]. In these systems, the ordering parameters of these lattices have a sigmoidal dependence as a function of temperature, which plateaus below the spin liquid transition temperature.

In addition, we can predict the time scale of these dynamics from the homogeneous linewidth. From the data (figure 6.9), we see dephasing on the order of picoseconds. Because this time scale

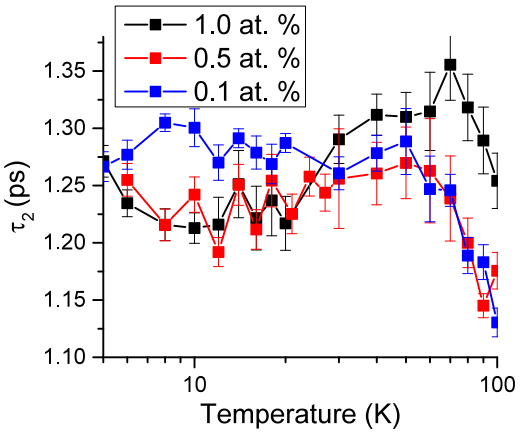

Figure 6.9: The low temperature dephasing time calculated from the homogeneous linewidth data for $R_1 \rightarrow Z_5$ emission from the D_2 site at all concentrations.

is much faster than the 50 Hz dynamics seen in the AC magnetic susceptibility data, we deduce this result is likely due to spin procession, which is a faster fluctuation than spin flipping in the J_z component of the total spin.

6.7 Spin Fluctuations as a Pure Dephasing Mechanism

In our model for the spin dynamics at low temperatures, the up and down states are degenerate in the spin liquid phase. Thus, dephasing caused by spin fluctuations should not cause energy to be

gained or lost by the Nd ions participating in the spin liquid phase. This mechanism should be a pure dephasing mechanism. The Raman scattering process would be an example of a process that is not purely dephasing because it is accompanied by energy shifts due to phonons sending the ion into a virtual vibronic state with a different energy than the pure electronic state. Therefore, by tracking the energy of the D_2 transition, we expect to see the effect of phonons at high temperature but no shifting due to the spin liquid coupling at low temperature.

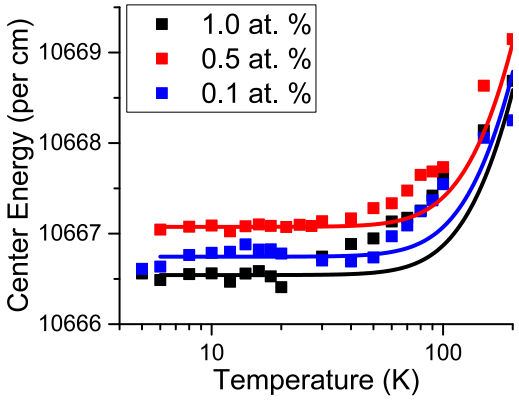

Figure 6.10: $R_1 \rightarrow Z_5$ center energy as a function of temperature and concentration from the D_2 site. The raw data are in squares and the expected behavior (solid lines) calculated using equation 3.34 with $T_D = 520\,\mathrm{K}$ and $W = 0.1$.

We have plotted that data in figure 6.10, which shows redshifting as a function of decreasing temperature, which is commensurate with the Raman scattering process. Furthermore, there is a high-temperature deviation between the data and the prediction based on of the Raman scattering model of Hsu and Skinner [34], which assumes the Debye approximation is correct. This deviation is likely due to thermal expansion and compression of the crystal [104], which modifies the phonon density of states. At low temperatures, we see that the center energy decreases to a constant value as expected. This confirms that we are seeing a pure dephasing mechanism in the form of neodymium-spin liquid coupling.

6.8 Conclusion & Future Direction

Optical detection of the effects of the spin liquid phase of GGG was demonstrated in the fluorescence of trivalent neodymium dopants. Coupling of neodymium to the gadolinium ions via a Heisenberg interaction allows spin fluctuations to affect the states of the neodymium. This manifests as a dephasing mechanism whose optical signature is homogeneous broadening of the natural line width with a simultaneous absence of energy shifting of the first excited-to-ground state transition. As the temperature of the GGG crystals is reduced, dephasing caused by phonons becomes negligible. Therefore, the only mechanism available for homogeneous broadening at low temperature is the presence of the spin liquid phase.

Future work based off of this experiment can go in several directions. GGG is still being studied to understand the structure of the spin protectorate phase present at 150 mK. To study this, the next step would be to repeat the presented measurement using ultra-low doping concentrations

in order to achieve single dopant detection using conventional optical methods [49]. This should be done in conjunction with a narrow line width, frequency stabilized, tunable laser as well as an ultra-high resolution spectrometer, which are needed to measure the true homogeneous linewidth of the Nd^{3+} emission which is likely on the order of kHz. In addition, a facility with a dilution refrigerator should be used to cool the GGG crystals through their spin protectorate phase so Nd-spin protectorate coupling can be studied. Finally, if coupling between Nd ions and spin protectorates can be confirmed, this material could potentially be used for quantum information processing. The narrow line width laser could be used for spin echo type measurements which would be the basis for a protocol to read and write information to the spin protectorates, similar to the optical protocol for addressing quantum memories made with rare earth doped ceramics [54].

Studies of other spin liquid materials via rare earth probing would be beneficial for the advancement of our understanding of geometrically frustrated magnetic systems, particularly of magnetic dynamics. The method detailed here could also be used to identify spin liquid behavior in other materials. These studies would be particularly important because there are currently only a handful of materials known to posses a frustrated magnetic phase and these materials have the potential to be the basis for quantum information processors [51].

In conclusion, we doped the geometrically frustrated magnet, gadolinium gallium garnet, with low concentrations of trivalent neodymium. The neodymium coupled to the frustrated magnetic lattice via a Heisenberg interaction. This resulted in the spin fluctuations inherent in the spin liquid phase to act as a dephasing mechanism, which homogeneously broadens the Nd emission. The homogeneous linewidth indicates that the time scale of the spin dynamics of GGG are on the order of 1.2 ps and that spin liquid correlations develop as microstates of the lattice well above the 2 K paramagnetic-to-spin liquid phase transition temperature.

Appendix A

Common Spectroscopy Lineshape Functions

A.1 Lorentzian Distribution

This function typically describes the intensity of a dipole, quadrapole, etc. transition as a function of frequency.

$$L(x; x_0, \Gamma, A) = \frac{A}{\pi} \frac{\Gamma/2}{(x - x_0)^2 + (\Gamma/2)^2} \tag{A.1}$$

x_0 is the position of the peak of the distribution.

Γ is the FWHM.

A is the total area of the distribution.

A.2 Fano Distribution

This function arises in situations when a system with discrete energy levels, like a quantum dot, couples to a system with a continuum of energy levels, like phonons in a crystal. It is important to note that the scaling parameter Ξ does not necessarily represent the area of the distribution because it is possible for the area to be unbounded for certain values of q. The Fano distribution reduces to the Lorentzian distribution when $q \to \infty$.

$$F(x; x_0, \Gamma, q, \Xi) = \Xi \frac{(q(\Gamma/2) + x - x_0)^2}{(\Gamma/2)^2 + (x - x_0)^2} \tag{A.2}$$

x_0 is the position of the peak of the distribution.

Γ is the FWHM.

Ξ is a scaling factor.

q is called the Fano parameter.

A.3 Gaussian Distribution

The Gaussian or normal distribution arises in many areas of science, particularly because the central limit theorem applies to many measurements. In spectroscopy, it is often seen when a random process acts on an ensemble of emitters, the most famous example being Doppler broadening.

$$G(x; x_0, \sigma, A) = A \exp\left(-\frac{(x - x_0)^2}{2\sigma^2}\right) \tag{A.3}$$

x_0 is the position of the peak of the distribution.

σ is the standard distribution of the distribution.

A is the total area of the distribution.

The full width at half maximum of the Gaussian distribution is

$$\Upsilon = \sigma\sqrt{8\ln(2)}. \tag{A.4}$$

A.4 Voigt Distribution

The Voigt distribution generalizes the Lorentzian and Gaussian distributions allowing one to model ensembles of emitters that are being acted upon by random processes.

$$V(x; x_0, \Gamma, \sigma, A) = \int_{-\infty}^{\infty} G(x')L(x - x')\mathrm{d}x' \tag{A.5}$$

$$= A\frac{\mathrm{Re}[w(z)]}{\sigma\sqrt{2\pi}} \tag{A.6}$$

where

$$z = \frac{(x - x_0) + i\Gamma/2}{\sigma\sqrt{2}} \tag{A.7}$$

$w(z)$ is the Faddeeva function.

x_0 is the position of the peak of the distribution.

σ is the standard deviation of the distribution, also called the Gaussian width.

Γ is the Lorentzian FWHM.

A is the total area of the distribution.

A.5 Fano-Gaussian Distribution

Like the Voigt distribution, the Fano-Gaussian distribution allows one to model inhomogeneously broadened emission from systems experiencing Fano resonance, which is often seen in Raman spectroscopy. Note that as the Fano parameter $q \to \infty$, the Fano-Gaussian distribution approaches the Voigt distribution as we would expect.

$$FG(x; x_0, \Gamma, \sigma, q, \Xi) = \int_{-\infty}^{\infty} G(x')F(x - x')\mathrm{d}x' \tag{A.8}$$

$$= \frac{A}{\sigma\sqrt{2\pi}}\left\{\left[1 - \frac{1}{q^2}\right]\mathrm{Re}[w(z)] - \frac{2}{q}\,\mathrm{Im}[w(z)]\right\} \tag{A.9}$$

where

$$z = \frac{(x - x_0) + i\Gamma/2}{\sigma\sqrt{2}} \tag{A.10}$$

$w(z)$ is the Faddeeva function.

x_0 is the position of the peak of the distribution.

σ is the standard deviation of the distribution, also called the Gaussian width.

Γ is the Lorentzian FWHM.

q is the Fano parameter.

Ξ is a scaling parameter.

A.6 Log-Normal Distribution

The log-normal distribution is an asymmetric distribution typically associated with particle size scaling in solutions.

$$LN(x; \mu, \sigma, A) = \frac{A}{x\sigma\sqrt{2\pi}}\exp\left(-\frac{[\log(x) - \mu]^2}{2\sigma^2}\right),\ x > 0 \tag{A.11}$$

μ is the location parameters of the peak.

σ is the width parameter of the peak.

A is the area of the distribution.

Bibliography

[1] Leon Balents. Spin liquids in frustrated magnets. *Nature*, 464(7286):199–208, March 2010. ISSN 0028-0836. doi: 10.1038/nature08917. URL http://www.nature.com/doifinder/10.1038/nature08917.

[2] David W. Ball. *The Basics of Spectroscopy*. The Society of Photo-Optical Instrumentation Engineers, Bellingham, 2001. ISBN 9780819478863. doi: 10.1117/3.422981.

[3] David Warren Ball. *Field guide to spectroscopy*. The Society of Photo-Optical Instrumentation Engineers, 2006. ISBN 0819463523. doi: 10.1117/3.682726. URL http://books.google.com/books?id=D8Dtj_TV1TIC&pgis=1.

[4] A. Barenco and M. A. Dupertuis. Quantum many-body states of excitons in a small quantum dot. *Physical Review B*, 52(4):2766–2778, July 1995. ISSN 0163-1829. doi: 10.1103/PhysRevB.52.2766. URL http://link.aps.org/doi/10.1103/PhysRevB.52.2766.

[5] Michael Bass. *Handbook of Optics: Volume I - Fundamentals, Techniques, & Design*. McGraw-Hill , Inc., New York, second edition, 1995. ISBN 0-07-047740-7.

[6] Michael Bass. *Handbook of Optics: Volume II - Device, Measurements, & Properties*. McGraw-Hill , Inc., New York, second edition, 1995. ISBN 0-07-047974-7.

[7] Wolfgang Becker. *Advanced Time-Correlated Single Photon Counting Applications*, volume 111 of *Springer Series in Chemical Physics*. Springer International Publishing, Cham, 2015. ISBN 978-3-319-14928-8. doi: 10.1007/978-3-319-14929-5. URL http://link.springer.com/10.1007/978-3-319-14929-5.

[8] George Bekefi and Alan H. Barrett. *Electromagnetic Vibrations, Waves, and Radiation*. The Mit Press, 1977.

[9] D W B Brace, P Prevost, B Stewart, G Kirchhoff, and R Bunsen. *The Laws of Radiation and Absorption: Memoirs by Prévost, Stewart, Kirchhoff, and Kirchhoff and Bunsen*. Harper's scientific memoirs. American Book Company, 1901. URL https://books.google.com/books?id=3KwRAAAAYAAJ.

[10] Michael Bradley. Curve fitting in raman and IR spectroscopy: Basic theory of line shapes and applications. Technical report, Thermo Fisher Scientific, Madison, 2007. URL http://www.thermoscientific.com/content/dam/tfs/ATG/CAD/CADDocuments/

Application&TechnicalNotes/MolecularSpectroscopy/Raman/RamanInstruments/AN50733_E.pdf.

[11] B H Bransden and C J Joachain. *Physics of Atoms and Molecules*. Pearson Education. Prentice Hall, 2003. ISBN 9780582356924. URL https://books.google.com/books?id=ST_DwIGZeTQC.

[12] S.V. Bulyarskii and V.V. Prikhodko. A Simple Theory of the Mn^{4+} R-Line Shape in Gadolinium Gallium Garnet. *physica status solidi (b)*, 222(2):563–568, November 2000. ISSN 0370-1972. doi: 10.1002/1521-3951(200011)222:2<563::AID-PSSB563>3.0.CO;2-L. URL http://doi.wiley.com/10.1002/1521-3951(200011)222:2<563::AID-PSSB563>3.0.CO;2-L.

[13] Kenny Chou and Allison Dennis. Förster resonance energy transfer between quantum dot donors and quantum dot acceptors. *Sensors*, 15(6):13288–13325, June 2015. ISSN 1424-8220. doi: 10.3390/s150613288. URL http://www.mdpi.com/1424-8220/15/6/13288/.

[14] S.W. Clark, J.M. Harbold, and F.W. Wise. Resonant Energy Transfer in PbS Quantum Dots. *Journal of Physical Chemistry C*, 111(20):7302–7305, May 2007. ISSN 1932-7447. doi: 10.1021/jp0713561. URL http://pubs.acs.org/cgi-bin/doilookup/?10.1021/jp0713561.

[15] B. Daudin, R. Lagnier, and B. Salce. Thermodynamic properties of the gadolinium gallium garnet, $gd_3ga_5o_{12}$, between 0.05 and 25 k. *Journal of Magnetism and Magnetic Materials*, 27(3):315–322, June 1982. ISSN 03048853. doi: 10.1016/0304-8853(82)90092-0. URL http://linkinghub.elsevier.com/retrieve/pii/0304885382900920.

[16] H. De Leebeeck and C. Görller-Walrand. Spectroscopic and magnetic properties of Nd^{3+} in $LiYF_4$. *Journal of Alloys and Compounds*, 225(1-2):75–79, 1995. ISSN 09258388. doi: 10.1016/0925-8388(94)07012-1. URL http://www.sciencedirect.com/science/article/pii/0925838894070121.

[17] M S Dresselhaus, G Dresselhaus, and A Jorio. *Group Theory - Application to the Physics of Condensed Matter*. Springer Berlin Heidelberg, 2008. ISBN 978-3-540-32899-8. doi: 10.1007/978-3-540-32899-8. URL http://www.springerlink.com/content/978-3-540-32897-1/.

[18] Charles Evans, Richard Brundle, and Shaun Wilson. *Encyclopedia of Materials Characterization*. Manning Publications Co., Greenwich, 1992. ISBN 978-0-08-052360-6. URL http://www.sciencedirect.com/science/book/9780080523606.

[19] C. G. L. Ferri, R. H. Inman, B. Rich, A. Gopinathan, M. Khine, and S. Ghosh. Plasmon-induced enhancement of intra-ensemble fret in quantum dots on wrinkled thin films. *Optical Materials Express*, 3(3):383, March 2013. ISSN 2159-3930. doi: 10.1364/OME.3.000383. URL https://www.osapublishing.org/ome/abstract.cfm?uri=ome-3-3-383.

[20] R P Feynman, R B Leighton, and M L Sands. *The Feynman Lectures on Physics: Commemorative Issue*. Benjamin-Cummings Publishing Company, 1989. ISBN 9780201500646. URL https://books.google.com/books?id=8fA6MwEACAAJ.

[21] Chi-Cheng Fu, Anthony Grimes, Maureen Long, Christopher G. L. Ferri, Brent D. Rich, Somnath Ghosh, Sayantani Ghosh, Luke P. Lee, Ajay Gopinathan, and Michelle Khine. Tunable nanowrinkles on shape memory polymer sheets. *Advanced Materials*, 21(44): 4472–4476, November 2009. ISSN 09359648. doi: 10.1002/adma.200902294. URL http://doi.wiley.com/10.1002/adma.200902294.

[22] Toshiyuki Fujii, Takayuki Nagai, Nobuaki Sato, Osamu Shirai, and Hajimu Yamana. Electronic absorption spectra of lanthanides in a molten chloride: II. Absorption characteristics of neodymium(III) in various molten chlorides. *Journal of Alloys and Compounds*, 393(1-2):L1–L5, May 2005. ISSN 09258388. doi: 10.1016/j.jallcom.2004.10.013. URL http://www.sciencedirect.com/science/article/pii/S0925838804013544.

[23] S. Ghosh, T. F. Rosenbaum, and G. Aeppli. Macroscopic signature of protected spins in a dense frustrated magnet. *Physical Review Letters*, 101(15):157205, October 2008. ISSN 0031-9007. doi: 10.1103/PhysRevLett.101.157205. URL http://link.aps.org/doi/10.1103/PhysRevLett.101.157205.

[24] Benjamin David Goddard. *Mathematical Analysis of Quantum Chemical Models for Small Atoms*. PhD thesis, University of Warwick, 2007. URL https://spiral.imperial.ac.uk/handle/10044/1/6963.

[25] John E Greedan. Geometrically frustrated magnetic materials. In *Functional Oxides*, volume 11, pages 41–117. John Wiley & Sons, Ltd, Chichester, UK, June 2010. doi: 10.1002/9780470686072.ch2. URL http://doi.wiley.com/10.1002/9780470686072.ch2.

[26] D J Griffiths. *Introduction to Quantum Mechanics*. Pearson international edition. Pearson Prentice Hall, 2005. ISBN 9780131118928. URL https://books.google.com/books?id=-BsvAQAAIAAJ.

[27] Alberto P. Guimarães. *Principles of Nanomagnetism*. NanoScience and Technology. Springer Berlin Heidelberg, Berlin, Heidelberg, 2009. ISBN 978-3-642-01481-9. doi: 10.1007/978-3-642-01482-6. URL http://link.springer.com/10.1007/978-3-642-01482-6.

[28] D C Harris and M D Bertolucci. *Symmetry and Spectroscopy: An Introduction to Vibrational and Electronic Spectroscopy*. Dover Books on Chemistry Series. Dover Publications, 1978. ISBN 9780486661445. URL https://books.google.com/books?id=I3W6oSaRlMsC.

[29] F.-J. Haug, T. Soderstrom, O. Cubero, V. Terrazzoni-Daudrix, and C. Ballif. Plasmonic absorption in textured silver back reflectors of thin film solar cells. *Journal of Applied Physics*, 104(6):064509, 2008. ISSN 00218979. doi: 10.1063/1.2981194. URL http://scitation.aip.org/content/aip/journal/jap/104/6/10.1063/1.2981194.

[30] B. Henderson and G.F. Imbusch. *Optical Spectroscopy of Inorganic Solids*. Oxford University Press, Oxford, 2010. ISBN 9780199298624. URL https://books.google.com/books?id=_EypTNBm2aQC&dq=optical+spectroscopy+of+inorganic+solids+henderson+doi&source=gbs_navlinks_s.

[31] Y. Hosoe, R. Imura, R. Suzuki, and T. Ikeda. Garnet films for 64 Mb bubble memory devices. *IEEE Transactions on Magnetics*, 25(5):4254–4256, 1989. ISSN 00189464. doi: 10.1109/20.42586. URL http://ieeexplore.ieee.org/lpdocs/epic03/wrapper.htm?arnumber=42586.

[32] S. Hov, H Bratsberg, and AT Skjeltorp. Magnetic phase diagram of gadolinium gallium garnet. *Journal of Magnetism and Magnetic Materials*, 15-18:455–456, January 1980. ISSN 03048853. doi: 10.1016/0304-8853(80)91128-2. URL http://www.sciencedirect.com/science/article/pii/0304885380911282.

[33] D. Hsu and J. L. Skinner. On the thermal broadening of zero-phonon impurity lines in absorption and fluorescence spectra. *The Journal of Chemical Physics*, 81(4):1604, 1984. ISSN 00219606. doi: 10.1063/1.447874. URL http://scitation.aip.org/content/aip/journal/jcp/81/4/10.1063/1.447874.

[34] D. Hsu and J. L. Skinner. Nonperturbative theory of temperature-dependent optical dephasing in crystals. I. Acoustic or optical phonons. *The Journal of Chemical Physics*, 81(12):5471, 1984. ISSN 00219606. doi: 10.1063/1.447648. URL http://scitation.aip.org/content/aip/journal/jcp/81/12/10.1063/1.447648.

[35] D. Hsu and J. L. Skinner. Nonperturbative theory of temperature-dependent optical dephasing in crystals. II. Pseudolocal phonons. *The Journal of Chemical Physics*, 83(5):2097, 1985. ISSN 00219606. doi: 10.1063/1.449352. URL http://scitation.aip.org/content/aip/journal/jcp/83/5/10.1063/1.449352.

[36] D. Hsu and J. L. Skinner. Nonperturbative theory of temperature-dependent optical dephasing in crystals. III. Comparison with experiment. *The Journal of Chemical Physics*, 83(5):2107, 1985. ISSN 00219606. doi: 10.1063/1.449353. URL http://scitation.aip.org/content/aip/journal/jcp/83/5/10.1063/1.449353.

[37] D. Hsu and J. L. Skinner. Nonperturbative theory of temperature-dependent optical dephasing in crystals. IV. Microscopic model for pseudolocal phonons. *The Journal of Chemical Physics*, 87(1):54, 1987. ISSN 00219606. doi: 10.1063/1.453603. URL http://scitation.aip.org/content/aip/journal/jcp/87/1/10.1063/1.453603.

[38] Shaowu Huang and Leung Tsang. Subwavelength imaging of plasmon superlens with 3-dimensional small surface roughness. In *Proceedings of the 2012 IEEE International Symposium on Antennas and Propagation*, pages 1–2. IEEE, July 2012. ISBN 978-1-4673-0462-7. doi: 10.1109/APS.2012.6349268. URL http://ieeexplore.ieee.org/lpdocs/epic03/wrapper.htm?arnumber=6349268.

[39] T Ida, M Ando, and H Toraya. Extended pseudo-Voigt function for approximating the Voigt profile. *Journal of Applied Crystallography*, 33(6):1311–1316, December 2000. ISSN 0021-8898. doi: 10.1107/S0021889800010219. URL http://scripts.iucr.org/cgi-bin/paper?S0021889800010219.

[40] L B Ioffe, M V Feigel'man, A Ioselevich, D Ivanov, M Troyer, and G Blatter. Topologically protected quantum bits using Josephson junction arrays. *Nature*, 415(6871):503–506, January 2002. ISSN 00280836. doi: 10.1038/415503a. URL http://www.nature.com/doifinder/10.1038/415503a.

[41] Shinichi Itoh. *Ab Initio Calculations of Multiplet Terms for Rare Earth Ions*. Phd, University of Electro-Communications, 1993. URL http://flex.phys.tohoku.ac.jp/riron/ronbun/d93itoh.pdf.

[42] Jens Jensen and Allan R. Mackintosh. *Rare earth magnetism: structures and excitations*. Clarendon Press, Oxford, 1991. ISBN 9780198520276. URL http://ukcatalogue.oup.com/product/9780198520276.do.

[43] K Jin, N P Butch, K Kirshenbaum, J Paglione, and R L Greene. Link between spin fluctuations and electron pairing in copper oxide superconductors. *Nature*, 476(7358):73–75, August 2011. ISSN 0028-0836. doi: 10.1038/nature10308. URL http://www.nature.com/doifinder/10.1038/nature10308.

[44] Kotaro Kajikawa. *Optical Properties of Advanced Materials*, volume 168 of *Springer Series in Materials Science*. Springer Berlin Heidelberg, Berlin, Heidelberg, 2013. ISBN 978-3-642-33526-6. doi: 10.1007/978-3-642-33527-3. URL http://link.springer.com/10.1007/978-3-642-33527-3.

[45] Yehoshua Y. Kalisky. *Solid State Lasers: Tunable Sources and Passive Q-Switching Elements*. The International Society for Optical Engineering, 2014. ISBN 9780819498212. doi: 10.1117/3.1002504. URL http://ebooks.spiedigitallibrary.org/book.aspx?doi=10.1117/3.1002504.

[46] Anne K. Kenworthy, Nadezda Petranova, and Michael Edidin. High-resolution FRET microscopy of cholera toxin B-subunit and GPI-anchored proteins in cell plasma membranes. *Molecular biology of the cell*, 11(5):1645–1655, 2000. ISSN 1059-1524. doi: 10.1091/mbc.11.5.1645. URL http://www.molbiolcell.org/content/11/5/1645.short.

[47] W. I. Kinney and W. P. Wolf. Magnetic interactions and short range order in gadolinium gallium garnet. *Journal of Applied Physics*, 50(B3):2115, 1979. ISSN 00218979. doi: 10.1063/1.326954. URL http://scitation.aip.org/content/aip/journal/jap/50/B3/10.1063/1.326954.

[48] G Kirchhoff and R Bunsen. XLII. Chemical analysis by spectrum-observations.Second memoir. *Philosophical Magazine Series 4*, 22(148):329–349, 1861. doi: 10.1080/14786446108643164. URL http://www.tandfonline.com/doi/abs/10.1080/14786446108643164.

[49] R Kolesov, K Xia, R Reuter, R Stöhr, A Zappe, J Meijer, P.R. Hemmer, and J Wrachtrup. Optical detection of a single rare-earth ion in a crystal. *Nature Communications*, 3(May): 1029, August 2012. ISSN 2041-1723. doi: 10.1038/ncomms2034. URL `http://www.nature.com/doifinder/10.1038/ncomms2034`.

[50] Takashi Kushida. Linewidths and thermal shifts of spectral lines in neodymium-doped yttrium aluminum garnet and calcium fluorophosphate. *Physical Review*, 185(2):500–508, September 1969. ISSN 0031-899X. doi: 10.1103/PhysRev.185.500. URL `http://journals.aps.org/pr/abstract/10.1103/PhysRev.185.500`.

[51] Claudine Lacroix, Philippe Mendels, and Frederic Mila. *Introduction to Frustrated Magnetism*, volume 164 of *Springer Series in Solid-State Sciences*. Springer Berlin Heidelberg, Berlin, Heidelberg, 2011. ISBN 978-3-642-10588-3. doi: 10.1007/978-3-642-10589-0. URL `http://link.springer.com/10.1007/978-3-642-10589-0`.

[52] Michael J. Lawler, Hae-Young Kee, Yong Baek Kim, and Ashvin Vishwanath. Topological Spin Liquid on the Hyperkagome Lattice of $Na_4Ir_3O_8$. *Physical Review Letters*, 100 (22):227201, June 2008. ISSN 0031-9007. doi: 10.1103/PhysRevLett.100.227201. URL `http://link.aps.org/doi/10.1103/PhysRevLett.100.227201`.

[53] Guokui Liu, Robert Hull, Jürgen Parisi, R. M. Osgood, Hans Warlimont, and Bernard Jacquier. *Spectroscopic Properties of Rare Earths in Optical Materials*, volume 83. Springer Berlin Heidelberg, 2005. ISBN 3-540-23886-7. doi: 10.1007/3-540-28209-2. URL `http://link.springer.com/10.1007/3-540-28209-2`.

[54] J. J. Longdell, M. J. Sellars, and N. B. Manson. Demonstration of Conditional Quantum Phase Shift Between Ions in a Solid. *Physical Review Letters*, 93(13):130503, September 2004. ISSN 0031-9007. doi: 10.1103/PhysRevLett.93.130503. URL `http://link.aps.org/doi/10.1103/PhysRevLett.93.130503`.

[55] Manuela Lunz, a. Louise Bradley, Wei-Yu Chen, Valerie a. Gerard, Stephen J. Byrne, Yurii K. Gunko, Vladimir Lesnyak, and Nikolai Gaponik. Influence of quantum dot concentration on förster resonant energy transfer in monodispersed nanocrystal quantum dot monolayers. *Physical Review B*, 81(20):205316, May 2010. ISSN 1098-0121. doi: 10.1103/PhysRevB.81.205316. URL `http://link.aps.org/doi/10.1103/PhysRevB.81.205316`.

[56] Manuela Lunz, A. Louise Bradley, Valerie a. Gerard, Stephen J. Byrne, Yurii K. Gunko, Vladimir Lesnyak, and Nikolai Gaponik. Concentration dependence of förster resonant energy transfer between donor and acceptor nanocrystal quantum dot layers: Effect of donor-donor interactions. *Physical Review B*, 83(11):115423, March 2011. ISSN 1098-0121. doi: 10.1103/PhysRevB.83.115423. URL `http://link.aps.org/doi/10.1103/PhysRevB.83.115423`.

[57] Rajni Mahajan, AL Shah, Suranjan Pal, and Anil Kumar. Analytical study for investigating the behaviour of Nd-doped Glass, YAG and GGG under the heat capacity mode of operation. *Optics & Laser Technology*, 39(7):1406–1412, October 2007. ISSN 00303992.

doi: 10.1016/j.optlastec.2006.10.008. URL http://www.sciencedirect.com/science/article/pii/S0030399206002064.

[58] Stefan A. Maier. *Plasmonics: Fundamentals and Applications*. Springer US, Boston, MA, 2007. ISBN 978-0-387-33150-8. doi: 10.1007/0-387-37825-1. URL http://link.springer.com/10.1007/0-387-37825-1.

[59] Marco Marceddu, Marianna Manca, Pier Carlo Ricci, and Alberto Anedda. The temperature dependence of Cr^{3+}:YAG zero-phonon lines. *Journal of physics. Condensed matter : an Institute of Physics journal*, 24(13):135401, April 2012. ISSN 1361-648X. doi: 10.1088/0953-8984/24/13/135401. URL http://iopscience.iop.org/0953-8984/24/13/135401.

[60] I M Marshall, S J Blundell, F L Pratt, A Husmann, C a Steer, a I Coldea, W Hayes, and R C C Ward. A muon-spin relaxation (tSR) study of the geometrically frustrated magnets Gd 3 Ga 5 O 12 and ZnCr 2 O 4. *Journal of Physics: Condensed Matter*, 14(6):L157–L163, February 2002. ISSN 0953-8984. doi: 10.1088/0953-8984/14/6/104. URL http://iopscience.iop.org/0953-8984/14/6/104.

[61] Dinesh Martien. Introduction to: AC Susceptibility. Technical report, Quantum Design. URL http://www.qdusa.com/sitedocs/appNotes/ppms/1078-201.pdf.

[62] B.R. Masters. Paths to Försters resonance energy transfer (FRET) theory. *The European Physical Journal H*, 39(1):87–139, February 2014. ISSN 2102-6459. doi: 10.1140/epjh/e2013-40007-9. URL http://link.springer.com/article/10.1140/epjh/e2013-40007-9.

[63] Koichi Momma and Fujio Izumi. Vesta 3 for three-dimensional visualization of crystal, volumetric and morphology data. *Journal of Applied Crystallography*, 44(6):1272–1276, 2011. ISSN 00218898. doi: 10.1107/S0021889811038970.

[64] J W Morris. A survey of materials science, 2007. URL http://www.mse.berkeley.edu/groups/morris/MSE200/I-structure.pdf.

[65] Michiel Müller. *Introduction to Confocal Fluorescence Microscopy, Second Edition*. SPIE, Bellingham, 2nd edition, December 2005. ISBN 9780819460431. doi: 10.1117/3.639736. URL http://ebooks.spiedigitallibrary.org/book.aspx?doi=10.1117/3.639736.

[66] J. Nasu, T. Kaji, K. Matsuura, M. Udagawa, and Y. Motome. Finite-temperature phase transition to a quantum spin liquid in a three-dimensional kitaev model on a hyperhoneycomb lattice. *Physical Review B*, 89(11):115125, March 2014. ISSN 1098-0121. doi: 10.1103/PhysRevB.89.115125. URL http://link.aps.org/doi/10.1103/PhysRevB.89.115125.

[67] Chetan Nayak, Steven H. Simon, Ady Stern, Michael Freedman, and Sankar Das Sarma. Non-Abelian anyons and topological quantum computation. *Reviews of Modern Physics*, 80(3):1083–1159, September 2008. ISSN 0034-6861. doi: 10.1103/RevModPhys.80.1083. URL http://link.aps.org/doi/10.1103/RevModPhys.80.1083.

[68] I Newton. *Opticks, Or, A Treatise of the Reflections, Refractions, Inflections & Colours of Light*. Dover books on history of science and classics of science. Dover Publications, 1979. ISBN 9780486602059. URL http://www.gutenberg.org/ebooks/33504.

[69] Wolfgang Nolting and Anupuru Ramakanth. *Quantum Theory of Magnetism*. Springer Berlin Heidelberg, Berlin, Heidelberg, 2009. ISBN 978-3-540-85415-9. doi: 10.1007/978-3-540-85416-6. URL http://link.springer.com/10.1007/978-3-540-85416-6.

[70] O. A. Petrenko, C Ritter, M Yethiraj, and D. McK Paul. Investigation of the low-temperature spin-liquid behavior of the frustrated magnet gadolinium gallium garnet. *Physical Review Letters*, 80(20):4570–4573, May 1998. ISSN 0031-9007. doi: 10.1103/PhysRevLett.80.4570. URL http://journals.aps.org/prl/abstract/10.1103/PhysRevLett.80.4570.

[71] O.A Petrenko, D.McK Paul, C Ritter, T Zeiske, and M Yethiraj. Magnetic frustration and order in gadolinium gallium garnet. *Physica B: Condensed Matter*, 266(1-2):41–48, May 1999. ISSN 09214526. doi: 10.1016/S0921-4526(98)01490-2. URL http://linkinghub.elsevier.com/retrieve/pii/S0921452698014902.

[72] Ch. Pfistner, P. Albers, W. Lüthy, and H.P. Weber. Thermal dependence of fluorescence lines of Er3+ in YAlO3. *Physics Letters A*, 137(9):457–462, June 1989. ISSN 03759601. doi: 10.1016/0375-9601(89)90225-9. URL http://linkinghub.elsevier.com/retrieve/pii/0375960189902259.

[73] Richard C Powell. *Symmetry, Group Theory, and the Physical Properties of Crystals*, volume 824 of *Lecture Notes in Physics*. Springer New York, New York, NY, 2010. ISBN 978-1-4419-7597-3. doi: 10.1007/978-1-4419-7598-0. URL http://www.springerlink.com/index/10.1007/978-1-4419-7598-0.

[74] CNR Rao, PJ Thomas, and GU Kulkarni. *Nanocrystals: Synthesis, Properties and Applications*. Springer Berlin Heidelberg, Berlin, Heidelberg, 2007. ISBN 978-3-540-68751-1. doi: 10.1007/978-3-540-68752-8. URL http://www.springerlink.com/index/10.1007/978-3-540-68752-8.

[75] Jan N Reimers and A. J. Berlinsky. Order by disorder in the classical heisenberg kagomé antiferromagnet. *Physical Review B*, 48(13):9539–9554, October 1993. ISSN 0163-1829. doi: 10.1103/PhysRevB.48.9539. URL http://link.aps.org/doi/10.1103/PhysRevB.48.9539.

[76] Sangeeta Saini, Harjinder Singh, and Biman Bagchi. Fluorescence resonance energy transfer (FRET) in chemistry and biology: Non-Förster distance dependence of the FRET rate. *Journal of Chemical Sciences*, 118(1):23–35, January 2006. ISSN 0253-4134. doi: 10.1007/BF02708762. URL http://link.springer.com/10.1007/BF02708762.

[77] J. J. Sakurai. *Modern Quantum Mechanics*. Addison-Wesley, Reading, revised edition, 1994. ISBN 9780805382914. doi: 10.1119/1.14491. URL http://link.aip.org/link/?AJP/54/668/1&Agg=doi.

[78] Haruo Sawada. Electron Density Study of Garnets:$Z_3Ga_5O_{12}$;Z=Nd, Sm, Gd, Tb. *Journal of Solid State Chemistry*, 132(2):300–307, September 1997. ISSN 00224596. doi: 10.1006/jssc.1997.7462. URL http://linkinghub.elsevier.com/retrieve/pii/S0022459697974624.

[79] P Schiffer, A. P. Ramirez, D. A. Huse, and A. J. Valentino. Investigation of the Field Induced Antiferromagnetic Phase Transition in the Frustrated Magnet: Gadolinium Gallium Garnet. *Physical Review Letters*, 73(18):2500–2503, October 1994. ISSN 0031-9007. doi: 10.1103/PhysRevLett.73.2500. URL http://link.aps.org/doi/10.1103/PhysRevLett.73.2500.

[80] P. Schiffer, A. P. Ramirez, D. A. Huse, P. L. Gammel, U. Yaron, D. J. Bishop, and A. J. Valentino. Frustration induced spin freezing in a site-ordered magnet: Gadolinium gallium garnet. *Physical Review Letters*, 74(12):2379–2382, March 1995. ISSN 0031-9007. doi: 10.1103/PhysRevLett.74.2379. URL http://link.aps.org/doi/10.1103/PhysRevLett.74.2379.

[81] George H. Seward. *Optical Design of Microscopes*. SPIE, 1000 20th Street, Bellingham, WA 98227-0010 USA, April 2010. ISBN 9780819480958. doi: 10.1117/3.855480. URL http://ebooks.spiedigitallibrary.org/book.aspx?doi=10.1117/3.855480.

[82] R D Shannon. Revised effective ionic radii and systematic studies of interatomic distances in halides and chalcogenides. *Acta Crystallographica Section A*, 32(5):751–767, September 1976. ISSN 0567-7394. doi: 10.1107/S0567739476001551. URL http://scripts.iucr.org/cgi-bin/paper?S0567739476001551.

[83] Bhavya Sharma, Renee R. Frontiera, Anne-Isabelle Henry, Emilie Ringe, and Richard P. Van Duyne. SERS: Materials, applications, and the future. *Materials Today*, 15(1-2):16–25, January 2012. ISSN 13697021. doi: 10.1016/S1369-7021(12)70017-2. URL http://linkinghub.elsevier.com/retrieve/pii/S1369702112700172.

[84] G. V. Shcherbatyuk, R. H. Inman, and S. Ghosh. Anomalous photo-induced spectral changes in CdSe/ZnS quantum dots. *Journal of Applied Physics*, 110(5):053518, 2011. ISSN 00218979. doi: 10.1063/1.3630977. URL http://scitation.aip.org/content/aip/journal/jap/110/5/10.1063/1.3630977.

[85] J.-E. Shea, J N Onuchic, and C L Brooks. Exploring the origins of topological frustration: Design of a minimally frustrated model of fragment B of protein A. *Proceedings of the National Academy of Sciences*, 96(22):12512–12517, October 1999. ISSN 0027-8424. doi: 10.1073/pnas.96.22.12512. URL http://www.pnas.org/cgi/doi/10.1073/pnas.96.22.12512.

[86] Robin A Swainson and G W F Drake. A unified treatment of the non-relativistic and relativistic hydrogen atom I: The wavefunctions. *Journal of Physics A: Mathematical and General*, 24(1):79–94, 1999. ISSN 0305-4470. doi: 10.1088/0305-4470/24/1/019. URL http://iopscience.iop.org/0305-4470/24/1/019.

[87] Henryk Szmacinski, Krishanu Ray, and Joseph R. Lakowicz. Effect of plasmonic nanostructures and nanofilms on fluorescence resonance energy transfer. *Journal of Biophotonics*, 2 (4):243–252, April 2009. ISSN 1864063X. doi: 10.1002/jbio.200910003. URL `http://doi.wiley.com/10.1002/jbio.200910003`.

[88] Valerii Ter-Mikirtychev. *Fundamentals of fiber lasers and fiber amplifiers*, volume 181. Spinger, Cham, 2014. ISBN 9783319023373. doi: 10.1007/978-3-319-02338-0-9.

[89] Michael Tinkham. *Group theory and quantum mechanics*. Dover Publications, New York, 1964. ISBN 9780486432472. URL `http://store.doverpublications.com/0486720446.html`.

[90] Andrei Tokmakoff. Time-dependent quantum mechanics and spectroscopy. 2014. URL `https://tdqms.uchicago.edu/`.

[91] Kosmas L. Tsakmakidis, Tim W. Pickering, Joachim M. Hamm, a. Freddie Page, and Ortwin Hess. Completely Stopped and Dispersionless Light in Plasmonic Waveguides. *Physical Review Letters*, 112(16):167401, April 2014. ISSN 0031-9007. doi: 10.1103/PhysRevLett.112.167401. URL `http://link.aps.org/doi/10.1103/PhysRevLett.112.167401`.

[92] Martin Vacha. Topics in molecular photophysics and spectroscopy. URL `http://www.op.titech.ac.jp/lab/vacha/English/Downloads/index.html`.

[93] A P Vink and A Meijerink. Electron-phonon coupling of Cr^{3+} doped garnets. *Journal of Physics and Chemistry of Solids*, 61(10):1717–1725, 2000. ISSN 00223697. doi: 10.1016/S0022-3697(00)00047-0. URL `http://www.sciencedirect.com/science/article/pii/S0022369700000470`.

[94] Michael Wahl. Time-correlated single photon counting. Technical report, PicoQuant, 2014. URL `http://www.picoquant.com/images/uploads/page/files/7253/technote_tcspc.pdf`.

[95] S. Wang, S. Boussaad, and N. J. Tao. Surface plasmon resonance enhanced optical absorption spectroscopy for studying molecular adsorbates. *Review of Scientific Instruments*, 72(7):3055, 2001. ISSN 00346748. doi: 10.1063/1.1379604. URL `http://scitation.aip.org/content/aip/journal/rsi/72/7/10.1063/1.1379604`.

[96] M. J. Weber and T. E. Varitimos. Optical Spectra and Intensities of Nd^{3+} in $YAlO_3$. *Journal of Applied Physics*, 42(12):4996, 1971. ISSN 00218979. doi: 10.1063/1.1659885. URL `http://scitation.aip.org/content/aip/journal/jap/42/12/10.1063/1.1659885`.

[97] Zheng Wen-Chen, Li Bang-Xing, Feng Guo-Ying, and Liu Hong-Gang. Research on the thermal shifts and electron-phonon coupling parameters of R-line for Cr^{3+} and Mn^{4+} ions in $YAlO_3$ crystals. *Journal of Luminescence*, 138:214–217, June 2013. ISSN 00222313. doi: 10.1016/j.jlumin.2013.02.003. URL `http://linkinghub.elsevier.com/retrieve/pii/S0022231313000586`.

[98] Katherine A Willets and Richard P Van Duyne. Localized surface plasmon resonance spectroscopy and sensing. *Annual Review of Physical Chemistry*, 58(1):267–297, May

2007. ISSN 0066-426X. doi: 10.1146/annurev.physchem.58.032806.104607. URL http://www.annualreviews.org/doi/abs/10.1146/annurev.physchem.58.032806.104607.

[99] N Woo, D M Silevitch, C Ferri, S Ghosh, and T F Rosenbaum. Interplay of disorder and geometrical frustration in doped gadolinium gallium garnet. *Journal of Physics: Condensed Matter*, 27(29):296001, July 2015. ISSN 0953-8984. doi: 10.1088/0953-8984/27/29/296001. URL http://stacks.iop.org/0953-8984/27/i=29/a=296001.

[100] Darwin L Wood and Kurt Nassau. Optical properties of gadolinium gallium garnet. *Applied Optics*, 29(25):3704, September 1990. ISSN 0003-6935. doi: 10.1364/AO.29.003704. URL https://www.osapublishing.org/ao/abstract.cfm?uri=ao-29-25-3704.

[101] Frederick Wooten. *Optical Properties of Solids*. Academic Press, New York, 1972. ISBN 978-1483207339.

[102] Taras Yavorskii, Matthew Enjalran, and Michel J P Gingras. Spin Hamiltonian, Competing Small Energy Scales, and Incommensurate Long-Range Order in the Highly Frustrated $Gd_3Ga_5O_{12}$. *Physical Review Letters*, 97(26):267203, December 2006. ISSN 0031-9007. doi: 10.1103/PhysRevLett.97.267203. URL http://link.aps.org/doi/10.1103/PhysRevLett.97.267203.

[103] Peter Y Yu and Manuel Cardona. *Fundamentals of Semiconductors*. Graduate Texts in Physics. Springer Berlin Heidelberg, Berlin, Heidelberg, 2010. ISBN 978-3-642-00709-5. doi: 10.1007/978-3-642-00710-1. URL http://link.springer.com/10.1007/978-3-642-00710-1.

[104] W. C. Zheng, P. Su, and H. G. Liu. Static contribution to thermal shifts of spectral lines in gadolinium gallium garnet $Gd_3Ga_5O_{12}$:Nd^{3+} laser crystal. *Journal of Applied Physics*, 109(6):066103, 2011. ISSN 00218979. doi: 10.1063/1.3561488. URL http://scitation.aip.org/content/aip/journal/jap/109/6/10.1063/1.3561488.

[105] M. E. Zhitomirsky. Octupolar ordering of classical kagome antiferromagnets in two and three dimensions. *Physical Review B*, 78(9):094423, September 2008. ISSN 1098-0121. doi: 10.1103/PhysRevB.78.094423. URL http://link.aps.org/doi/10.1103/PhysRevB.78.094423.